Spectroscopy of Rubidium Plasma for Wakefield Diagnostics at the AWAKE Experiment

Helena Jaworska

University of Groningen

Spectroscopy of Rubidium Plasma
for Wakefield Diagnostics
at the AWAKE Experiment

Bachelor's Thesis

To fulfill the requirements for the degree of
Bachelor of Science in Physics and
Bachelor of Science in Applied Physics
at University of Groningen under the supervision of
dr. M. Turner (CERN)
and
prof. dr. ir. R.A. Hoekstra (Applied Physics, University of Groningen)
and
dr. M. Kavatsyuk (Physics, University of Groningen)

Helena Jaworska (s4819551)

August 13, 2024

Contents

Acknowledgments

Abstract

Previous work performed at the Stanford Linear Accelerator (SLAC) [1] showed that the light intensity of a lithium plasma line is proportional to the energy deposited in plasma by the driver when exciting wakefields. This thesis is focused on spectroscopy of rubidium plasma light to investigate wakefields created at the AWAKE experiment at CERN. This was done by measuring the intensity of multiple rubidium lines during wakefield excitation and comparing it to simulation results and expected line intensities from the NIST Atomic Spectrum Database. The main goals were to verify if the measurements agree with expectations, and to establish a correlation between the light intensity and plasma electron temperature. First, it was found that the simulations are only accurate for small propagation distances into the plasma, where linear theory applies. Second, it was determined the temperature of plasma cannot be accurately predicted by this type of measurement due to lack of understanding of behaviour of the plasma electrons due to the presence of wakefields. Lastly, plasma light measurements as a diagnostic for wakefield amplitude are only appropriate when observing a single transition. Further experiments are needed to look at the time-resolved spectrum of the plasma to provide insight into the evolution of plasma light. This could give information about the velocity distribution of plasma electrons and therefore their temperature.

1   Introduction

Particle accelerators have been an incredible tool scientists use to investigate the smallest elements of matter. The first particle accelerator, built in 1928 by Rolf Wideroe, was only two meters long, and it accelerated electrons to 50 keV [2]. The MeV range was reached only three years later with the first cyclotron [3]. The first GeV accelerator was built just a few years later, which led to the discovery of quarks and extensive study leptons, quarks, photons and gluons. Most recently, the crown jewel of particle accelerators, the Large Hadron Collider (LHC) was used to prove the existence of the Higgs boson, completing the standard model: the (currently) most comprehensive model of all physical interactions in the universe.

Since their inception particle accelerators have grown from mere two metres to over 27 kilometres. The current accelerators are still on the cutting edge of physics, but plans for yet larger accelerators are being made. An example of that is the CERN Future Circular Collider (FCC), which is supposed to have a staggering 90 kilometre diameter. While there are still scientific questions to be answered, the ever-growing accelerators are causing ever-growing concerns with regards to the costs, water and power use, disruption of farmlands and natural habitats, and the carbon footprint of the construction efforts [4, 5, 6]. These accelerators also have the limit, as the accelerating field can only get so high before it breaks down and starts causing damage to the equipment [7].

In this landscape, alternative technologies have the potential to blossom. One such technology is being developed at the AWAKE experiment at CERN, in Geneva. AWAKE stands for **A**dvanced **Wak**efield **E**xperiment, and it is an R&D experiment on plasma wakefield acceleration. At AWAKE, some of the electrons in a 10 metre long plasma are forced to oscillate by the field of an external beam of electrons or protons that propagates along the plasma axis. Their oscillation creates areas of high and low plasma electron density, and the resulting longitudinal fields can be used to accelerate charged particles. This method has the advantage of being able to provide much higher accelerating fields, in the range of GeV per metre, compared to MeV per metre in radio-frequency cavities used in conventional accelerators.

Currently, AWAKE is working on stabilising the amplitude of the high accelerating fields over long distances by changing the plasma density profile. One of the diagnostics used to analyse the effect of that density on the wakefields is plasma light spectrometry. It is expected that the amplitude of light emitted by the plasma depends on the amount of energy deposited to the plasma electrons by the driver bunch [8]. Therefore, studying the emission lines may provide information about the wakefields. By observing the plasma spectrum during and after wakefield excitation and comparing it to known spectral line intensities or ratios between their intensities, an approximation of the energy that was gained from the plasma fields could be made. This paper follows two research topics: a theoretical, simulation-based description of the evolution of wakefields in plasma, and an experimental investigation of spectral line intensities and relations between them. It aims to come to a conclusion about the relation between the wakefield amplitudes and the observed spectral lines.

1.1   Research Questions

To summarise, this thesis focuses on the following problems:

    Q1. How do the theoretical predictions for wakefield amplitude close to the plasma entrance align with experimental observations?

    Q2. How do ratios between different spectral lines of rubidium evolve with changing wakefield amplitude and what can be inferred from those ratios about the mechanism of energy

loss by plasma electrons? Is measuring the entire spectrum of plasma light an appropriate diagnostic for wakefield amplitude?

1.2   Thesis Outline

This thesis is the final requirement for completing a BSc in Physics and BSc in Applied Physics. The structure of the document has to reflect that, as required by the Board of Examiners at the University of Groningen. The background information and experimental methods sections are common for both subjects, since the information there applies to both hypotheses. The thesis then separates into a Physics and Applied Physics sections. Lastly, a common conclusion about the research questions is reached.

2   Background Literature

2.1   Plasma Properties

Plasma is a quasi-neutral gas of charged particles. It shows collective behaviour, which means the long range $(1/r)$ of Coulomb potential leads to non-local disturbances [9]. The overall behaviour of the plasma is the sum of behaviours of individual particles in it, subject to external and internal forces. The internal forces are the result of particle charge, as the particles can create charge imbalances and currents, and therefore electric and magnetic fields.

Overall, the number density of electrons is locally balanced with the number density of ions [10]. For equal ion and electron temperatures it can be said that

$$\frac{1}{2}m_e v_e^2 = \frac{1}{2}m_i v_i^2 = \frac{3}{2}k_B T_e \tag{1}$$

where m_e and m_i are the mass of the electron and mass of the ion, v_e and v_i are the electron and ion velocity, T_e is electron temperature and k_B is the Boltzmann constant.

After rearranging we find that the ratio of thermal speeds of ions and electrons is:

$$\frac{v_i}{v_e} = \sqrt{\frac{m_e}{m_i}} \tag{2}$$

which is approximately 0.023 for hydrogen or 0.0038 for rubidium, which is the gas used in this experiment. Therefore, plasma ions can be considered almost stationary compared to plasma electrons [11].

2.2   Plasma Oscillations

Since the plasma ion velocity is negligible on the scale of electron velocity, the electrons can oscillate in the ion background and the plasma frequency can be derived. Consider a flat sheet of plasma, where electrons are displaced from their original position by distance δ. This creates a "capacitor" with surface charge $\sigma_{\pm} = \pm e n_{pe}\delta$, resulting in an electric field

$$E = \frac{e n_{pe}\delta}{\varepsilon_0} \tag{3}$$

where E is the electric field, e is electron charge, n_{pe} is the plasma electron density and ε_0 is the vacuum permittivity. The electron is then accelerated back to the slab with a force

$$F = m_e \frac{\mathrm{d}v}{\mathrm{d}t} = -m_e \frac{\mathrm{d}^2\delta}{\mathrm{d}t^2} = -eE \tag{4}$$

which is meant to pull electrons back to their original position [12]. Due to their inertia the electrons will begin oscillating around their equilibrium position with ω_{pe}, called the plasma frequency.

By combining Eq. 3 and Eq. 4 the electron plasma frequency can be found to be

$$\omega_{pe} = \sqrt{\frac{e^2 n_{pe}}{\varepsilon_0 m_e}} \tag{5}$$

This equation depends on n_{pe}, the plasma electron density, and constants. Notably, the frequency does not depend on the wavenumber k, which means the group velocity (defined as $v_g = \mathrm{d}\omega/\mathrm{d}k$) is not defined. Therefore, the disturbance in the plasma cannot propagate if the plasma is cold. Additionally, the electric fields created due to the oscillation of electrons will have no effect either, since the number density of electrons and ions is the same in the infinite "capacitor" example that was used to find the frequency.

In reality, the plasma wave can propagate, due to two separate effects. First, since the plasma is finite there are fringing electric fields at the edges of the plasma, which will cause disturbances in the plasma surrounding them. Second, plasma oscillation can also propagate due to thermal motion of electrons.

If the plasma frequency ω_{pe} (Eq. 5) is smaller than the frequency of an incoming laser beam ω_0, then the characteristic timescale of the plasma response is longer than that of the laser. The plasma then cannot stop the radiation and plasma is considered under-dense. If $\omega_{pe} < \omega_0$ the plasma is over-dense the electrons are able to respond to the incoming radiation and shield it, causing reflection. If ω_0 is known it can be used to calculate the maximum electron density for which the plasma will still be under-dense, which is given by

$$n_{pe} = \frac{\omega_0^2 \varepsilon_0 m_e}{e^2} \tag{6}$$

Knowing if plasma is under- of over-dense is especially relevant in a plasma accelerator, since a laser can be used to either excite plasma or create an oscillation in it, as is explained in sections 2.4 and 2.6.

2.3   Relativistic Particles in Plasma

Plasma Based Particle Accelerators can be driven by a laser pulse (Laser Wakefield Acceleration: LWFA) or a charged particle bunch (Plasma Wakefield Accelerator: PWFA). For the experiments described in this thesis a charged particle bunch was used. The particle bunch is accelerated to highly relativistic velocities by a series of conventional accelerators and then sent into a plasma, where it causes some of the plasma electrons to oscillate. Before significant acceleration, each of the particles in the bunch has a radial electric field of

$$E = \frac{q}{4\pi\varepsilon_0} \frac{1}{r^2} \tag{7}$$

Since the particles are travelling at highly relativistic speeds as they have been accelerated, their electric field will change due to their speed being close to the speed of light. To understand this mechanism a simple example of two parallel flat sheets can be considered. They have opposite charge density $\sigma^{\pm}$, such that if we take a Gaussian surface enclosing one of the plates we find that the field between the plates will be $E = \sigma/\varepsilon_0$. If the plates are moving with respect to the observer with velocity v the dimension parallel to the velocity will contract. This means the Gaussian surfaces that encloses the plates will change. The charge that is being enclosed will stay constant, since it is a Lorentz invariant quantity [13].

According to Gauss's law

$$\int_{S(t)} \vec{E} \cdot \mathrm{d}\vec{a} = \int_{S'(t)} \vec{E}' \cdot \mathrm{d}\vec{a}' \tag{8}$$

which means $EA = E'A'$. By using this and Eq.3 it can be found that

$$E'_\perp = \gamma \frac{\sigma}{\varepsilon_0} = E_\perp \gamma \tag{9}$$

If the velocity was instead parallel to the normal of the plates the field would stay the same. This is due to no contraction occurring in that direction, which means both the enclosed charge and Gaussian surface stay the same.

In the case of the single charged particle the field parallel to velocity becomes $E_\parallel = E_r$ and the perpendicular field becomes $E_\perp = \gamma E_r$, which means $E_\perp \gg E_\parallel$ [14] for $\gamma \gg 1$. In the AWAKE experiment, the driver is a 400 GeV proton bunch with velocity $v_{p+} \approx 0.99997c$. Therefore, $\gamma = 427$, which means the fields are mostly transverse.

2.4   Field Ionisation

Plasma is created when electrons gain enough energy to be freed (ionised) from atoms they are bound to [15]. Ionisation can occur through collisions of fast particles with atoms, breakdown of atoms by applying a strong electric field, or by photoionization by electromagnetic radiation [16]. The mechanism used in this experiment is a mix of both field ionisation and photoionisation.

The first process occurring here is multi-photon ionisation. In typical photoionisation a photon with energy equal to the ionisation energy of the electron is absorbed, giving the energy to the electron and therefore ionising it. In multi-photon ionisation a few photons need to be absorbed to reach enough energy. In this experiment the photons have energy ≈ 1.6 eV, and the ionisation energy of the first Rb electron is ≈ 4.2 eV, so three photons are needed for ionisation. This makes the process more unlikely, as it requires the simultaneous absorption of three photons instead of one, but it is still achievable with a very intense laser [17].

The second process is field ionisation, where a strong electric field frees the electrons. In this experiment the strong field is applied by a very intense laser. The minimum laser intensity required for this process can be calculated based on the electric field of the atom. An isolated hydrogen particle will have an electric field given by Eq. 7. This field can also be described as atomic intensity, equal to

$$I_A = \frac{\varepsilon_0 c}{2} E_B^2 \qquad (10)$$

where E_B is the field at Bohr radius (defined as $a_B = 4\pi\hbar\varepsilon_0 / m_e e^2$ [18]). This means that plasma can be created by using a laser of intensity (or field) higher than this threshold value. As an example, the laser used at AWAKE has power 4.5 TW and intensity $\approx 6 \times 10^{18}$ W/m^2.

2.5   Spectral Lines of Plasma

Plasma can emit light through two main processes: radiative and collisional. The first includes transitions between bound states of the atom where an electron is excited or de-excites within the energy levels, and recombination and photoionisation, where an ionised electron becomes bound to an ion again and emits a photon, or it becomes ionised by absorbing a photon. The latter includes electron impact excitation, three-body recombination, and dielectric recombination and autoionisation.

The output intensity of a line caused by a transition from an upper level u to a lower level l is

$$I_{ul} = n(u)A_{ul} \qquad (11)$$

where I_{ul} is the output intensity, $n(u)$ is the population of the upper level and A_{ul} is the transition probability of the specific transition $u \rightarrow l$. The transition probability can be found on the NIST Atomic Spectra Database, but the population of the level will depend on the distribution electrons in the atom.

The average number of electrons in the upper state is defined by the Fermi-Dirac distribution, which is given by

$$\bar{n}_i(\varepsilon_i) = \frac{1}{\exp((\varepsilon_i - \mu)/k_BT) + 1} \tag{12}$$

In a limit of high temperature and low particle density, the distribution is well approximated by the Boltzmann distribution [19], if local thermal equilibrium has been reached. For a given transition wavelength the intensity of that line will be proportional to

$$\frac{n_u}{n_l} = \exp(\frac{\varepsilon_l - \varepsilon_u}{k_BT}) = \exp(\frac{-h\nu_{ul}}{k_BT}) \tag{13}$$

It can be assumed that the levels u and l are formed of a number of degenerate states, described by the statistical weight g_i where $g_i = 2J_i + 1$[20]. This means Eq. 13 can be generalised as

$$\frac{P_u}{P_l} = \frac{g_u}{g_l} \exp(\frac{-h\nu_{ul}}{k_BT}) \tag{14}$$

Where P_i is the probability of occupation of the lower or upper state. The same argument can be made for a ratio of two lines, where their ratio will be equal to

$$\frac{P_1'}{P_2'} = \frac{g_1}{g_2} \exp(\frac{-h\nu_1 + h\nu_2}{k_BT}) \tag{15}$$

where g_i are the ratios of g_u to g_l, P_i' are the ratios of occupation probabilities for each line, and ν_i are the frequencies of the lines.

From Eq. 14 and Eq. 15 it can be found that in a limit where $(\varepsilon_l - \varepsilon_u) \ll k_BT$ the intensity of the lines and the ratio of lines will be constant, but the T when they reach that limit will be different.

This means that when a local thermal equilibrium occurs and $(\varepsilon_l - \varepsilon_u) \ll k_BT$, the ratio of intensities of lines will be described by the population of the energy levels and their transition probabilities, as stated by Eq. 11:

$$\frac{I_1}{I_2} = \frac{n(1,u)}{n(2,u)} \frac{A_1}{A_2} \tag{16}$$

which can simplify further to only depend on the ratio of g_i (Eq. 14) and ratio of A_i if the population of the levels to be approximately equal.

Another way the ratios between the intensities of lines can be described is in the form of the absorption oscillator strength, f_{ij}. This parameter describes the relative absorption intensities of lines with the same lower level, so it can only be used when two particles share that level. The ratio of f_{ij} for two levels corresponds to the ratio of intensities of those levels.

2.6 Principles of Plasma Acceleration

In plasma wakefield acceleration longitudinal electric fields, created in plasma due to electron oscillations, can accelerate charged particles that propagate along those fields. As described in section 2.2, electrons displaced transversely from their equilibrium positions will be accelerated back towards the initial position and will begin oscillating with a frequency dependent on the plasma density. This acceleration is caused by a restoring force from the positively charged, non-evolving plasma ion background (see 2.1). The plasma electron oscillation can be started with an intense laser pulse or a dense bunch of charged particles. The first concept of a laser (LWFA) and beam driven (PWFA) accelerators
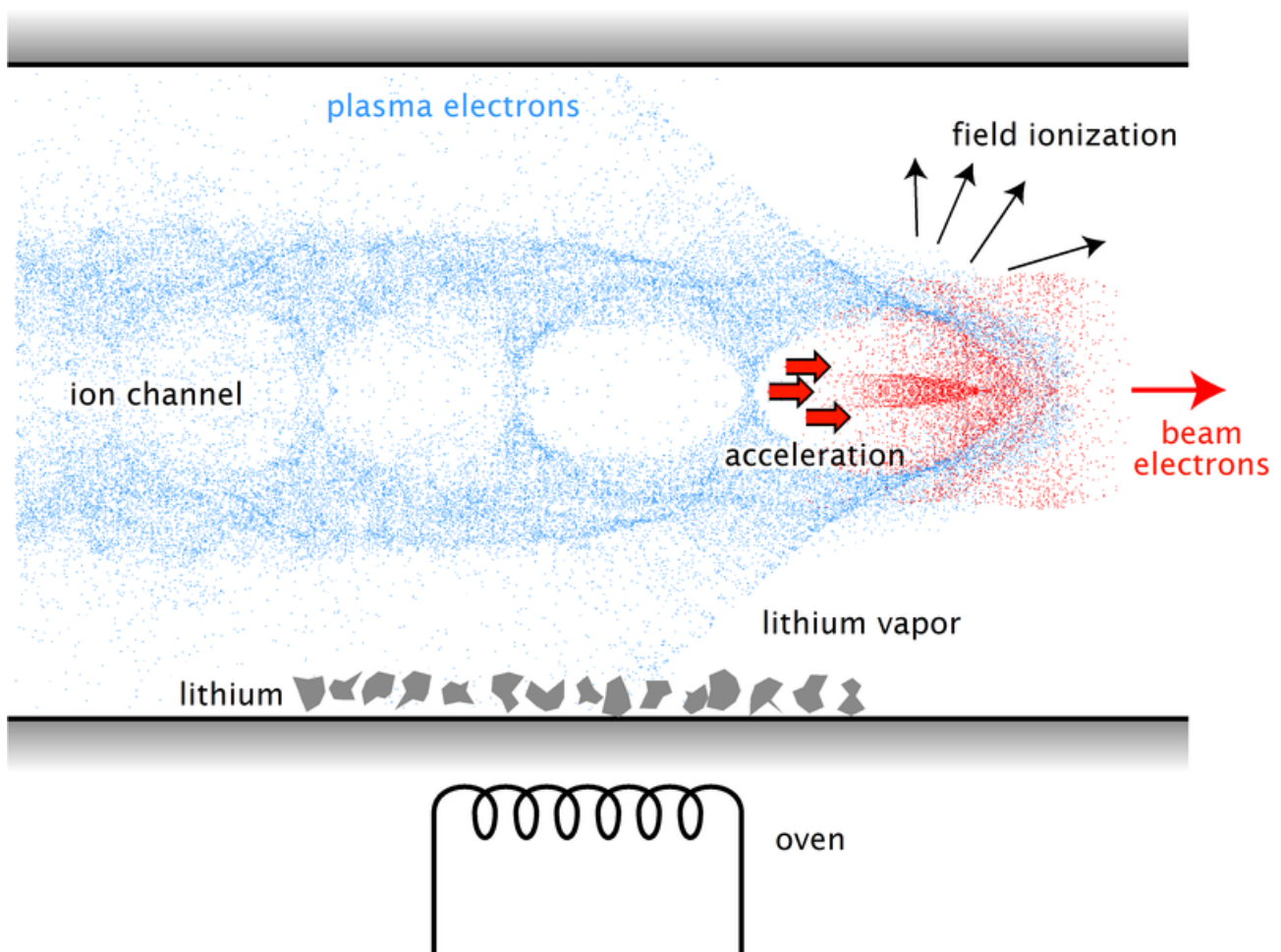
Figure 1: Illustration of the wakefield creation process. Here, the plasma is being both created and excited by a negatively charged driver (electron beam). Positively charged drivers can also be used. The plasma electrons are shown in blue, and the drive bunch electrons are shown in red. Image taken from [23], shared under the CC Attribution Share-Alike 3.0 license. Original image caption: *Illustration of the wake created by an electron beam in a plasma. This wake can be used to accelerate charged particles.* Author: Rasmus Ischebeck.

were published in 1979 [21] and 1985 [22], respectively.

In a PWFA a plasma oscillation is set up by injecting a high-charge particle bunch (called the drive bunch) into the plasma. In the case of a negatively charged drive bunch it displaces the electrons from the centre of the plasma. After the bunch passes the electrons are accelerated back due to the restoring force from the ions. Due to their inertia they overshoot the centre position and begin oscillating around the equilibrium. This is depicted in Fig. 1. This oscillation creates regions of focusing and defocusing fields transversely, and accelerating and decelerating fields longitudinally. Positively charged drivers have the same effect, but instead of pushing the electrons away from the centre they pull them towards it. When the force is removed (when the proton bunch passes) the electrons begin oscillating the same way they do with a negatively charged driver.

The relation between plasma light intensity and energy lost by the driver has been well established [8] and is widely used as a diagnostic for wakefield amplitude. However, the plasma light observed usually is a single spectral line, not the entire spectrum. The relationship between the total plasma light intensity and wakefields could be different, and is one of the main questions investigated in this

thesis.

2.6.1   Wake Breaking

The typical accelerating field in a plasma accelerator is given by the wave breaking field. It is the electric field amplitude that can be sustained by the plasma when all plasma electrons within a plasma skin-depth (c/ω_{pe}) are displaced by one skin depth [24]. This field was derived in 1959 by J. Dawson [25] to depend on the electron plasma frequency ω_{pe} and phase velocity as shown in Eq.17. The wake breaking field is

$$eE_{wb} = m_e\omega_{pe}v_{ph} = m_ec\sqrt{\frac{e^2n_{pe}}{\varepsilon_0 m_e}} \approx 100\sqrt{n_{pe}}\frac{\text{eV}}{\text{m}} \tag{17}$$

where n_{pe} is the plasma electron density in cm^{-3}. This means that the wave breaking field can reach around GeVm^{-1} for $n_{pe} > 10^{14}$cm^{-3}. The reason the field amplitude cannot increase past that point is that the paths of the electrons forming the wave will start to cross each other, therefore destroying the coherence of the wave. In plasma wakefield acceleration the wave breaking field calculated above can be exceeded, as the plasma oscillations are often only used for one oscillation period.
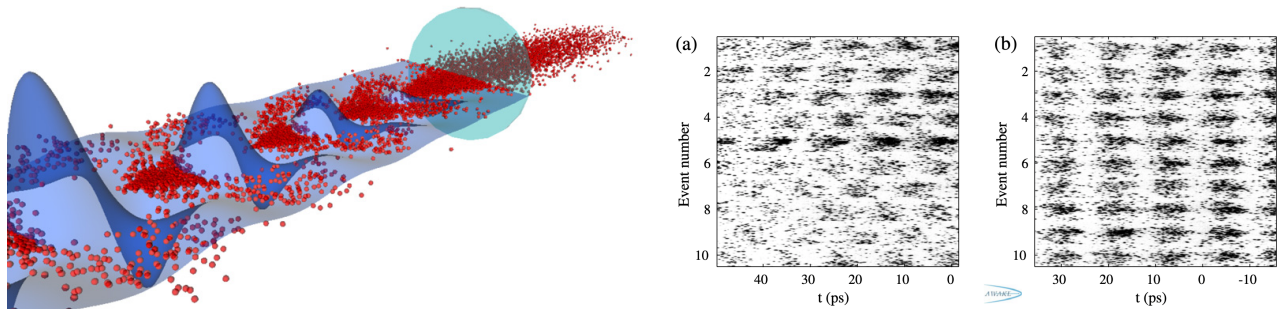
2.6.2   Self Modulation Instability

It was shown [26] that highest amplitude of accelerating amplitude is obtained when

$$\lambda_{pe} = \sqrt{2}\pi\sigma_z \tag{18}$$

(where σ_z is the bunch length and λ_{pe} is the plasma wavelength). This is also the case when the length of the drive bunch is on the order of the plasma wavelength ($\lambda_{pe} = 2\pi c/\omega_{pe}$). Longer drivers can also be used to excited wakefields, however, only after being formed into a train of short microbunches. One way of forming microbunches is self modulation instability (SMI). It is an instability which develops when a proton bunch with length $L > \lambda_{pe}$ enters a plasma [27]. The long drive bunch then induces a seed wakefield due to irregularities in its longitudinal profile. If the bunch was perfectly Gaussian the protons in the bunch would cancel out their individual contributions completely, leading to no wakefields created. The induced seed wakefields create a transverse field that propagates with the proton drive bunch, which focuses and de-focuses the proton bunch. This modulates the bunch, such that regions of higher and lower proton density occur [28] creating a train of microbunches. Since the bunch is modulated by wakefields with plasma frequency, which creates bunches with the same frequency, the wakefields are excited resonantly. The longitudinal field of the bunch is small due to the relativistic speeds of the bunch, so the modulation is mostly in the transverse direction of the bunch (see section 2.3). The longitudinal wakefields in plasma are therefore created by transverse defocusing of the bunch, which causes areas of high and low density, not by longitudinal modulation of the bunch. The longitudinal components of the wakefields can then be used to accelerate other particles.

2.6.3   Relative Ionisation Front and Seeded Self Modulation

The self modulation instability process is crucial when long drivers are used to excite a wakefield, as it allows much higher wakefields to be driven due to resonant excitation of multiple bunches. It was also found that the timing of the modulation can be controlled by choosing the charge density and amplitude of the bunch entering the plasma [31]. This is done by overlapping the laser pulse

(a) Simulation result of a proton bunch (red) resonantly driving a wakefield (blue). Plasma is created by a short laser pulse (teal circle). Figure was taken from [29], created by Alexey Petrenko, CERN.

(b) Difference between observed self modulation instability of a proton bunch (on the left) and seeded self modulation (on the right). The timing and amplitude of the bunches was shown to be reproducible when the wakefield amplitude is seeded (SSM). Figure taken from [30] under CC Attribution 4.0 International license.

Figure 2: Figures showing how a microbunch train resonantly excites wakefields (a) and the difference between the self modulation instability (SMI) and seeded self modulation (SSM) (b).

(which creates the plasma) with the drive bunch. Then, the plasma experiences a sudden increase of charge density, creating a "seed" wakefield. This process is therefore called Seeded Self Modulation (SSM). An impression of that process is shown in Fig. 2a. The comparison between the effect of SMI and SSM is shown in Fig. 2b. The amplitude of the wakefields that will be induced depends on the amplitude of the seeded wakefield (amplitude of the proton bunch at the position of the laser), the amount of protons in the plasma. Both the number of protons and the seed wakefield amplitude increases the amplitude of the wakefields that they induce over a given plasma length, but both of them cannot be maximised at the same time. The SSM process is controlled by changing the position of the laser with relation to the bunch, or the "Relative Ionisation Front" (RIF) position difference. RIF = 0 ps is defined as the laser pulse injected in the longitudinal centre of the proton bunch. It can be described as either position or timing. The position describes how far apart in space the laser and proton bunch are. The timing gives the time difference between the laser and the proton bunch. The RIF position difference can be converted into RIF timing difference by dividing by the speed of the proton bunch, which is (approximately) the speed of light.

2.7   Limitations of Plasma Acceleration

The main advantage of plasma acceleration over conventional acceleration is their large accelerating gradient. However, there are also challenges.

One of the issues specific to PWFA is dephasing. The phase velocity of the wakefields is defined by the group velocity of the driver bunch. The driver is slower than c and also decreasing its velocity because of the driving of the wakefields. The witness (accelerated) bunch does not lose energy, which means it can "outrun" the wakefield. This causes the witness bunch to experience smaller accelerating fields, and eventually decelerating ones. This can be rectified by increasing the density of plasma, as this will change the plasma wavelength to tune it to the changing length of the bunch.

Another issue is the beam quality. Electron beams accelerated PWFA accelerators usually have higher emittance than ones created during RF acceleration [32]. The drive and witness bunch also tend to increase in size as the distance travelled in the plasma increases [26]. Witness bunch emittance preservation can be achieved in plasma based accelerators when operating in the blow-out regime,

and was recently demonstrated experimentally with, however, a small energy gain [33].

2.8   AWAKE: Proton-Driven Plasma Wakefield Acceleration

AWAKE is a unique plasma wakefield acceleration experiment: instead of using an electron bunch or a laser beam to drive the wakefields, it uses a proton beam. This provides unique benefits and drawbacks.

First, the maximum achievable field gradient is [26]

$$E = 240(\text{MVm}^{-1})(\frac{N}{4 \times 10^{10}})(\frac{0.6}{\sigma_z(\text{mm})})^2 \tag{19}$$

where N is the number of particles in the driving bunch and σ_z is the length of the bunch (assuming a Gaussian profile). This means that the acceleration is proportional to the bunch population and inversely proportional to the bunch length. In a proton-driven accelerator the long bunch will split into microbunches (see section 2.6.2) and therefore reduce its length. However, this is not the main mechanism that leads to higher fields available, as the charge per bunch is drastically reduced when microbunches are formed. The high driven wakefields come from the resonant excitation of the wave by the many bunches.

Protons can be accelerated to TeV energies in conventional accelerators, which means they could be used as wakefield drivers to accelerate electrons to similar energies. Due to their large amount of stored energy, a proton-driven wakefield accelerator can reach higher electron energy gains than an electron- or laser-driven one [34]. This means that sufficient energy could be reached in a single stage, compared to multiple stages in other plasma accelerators.
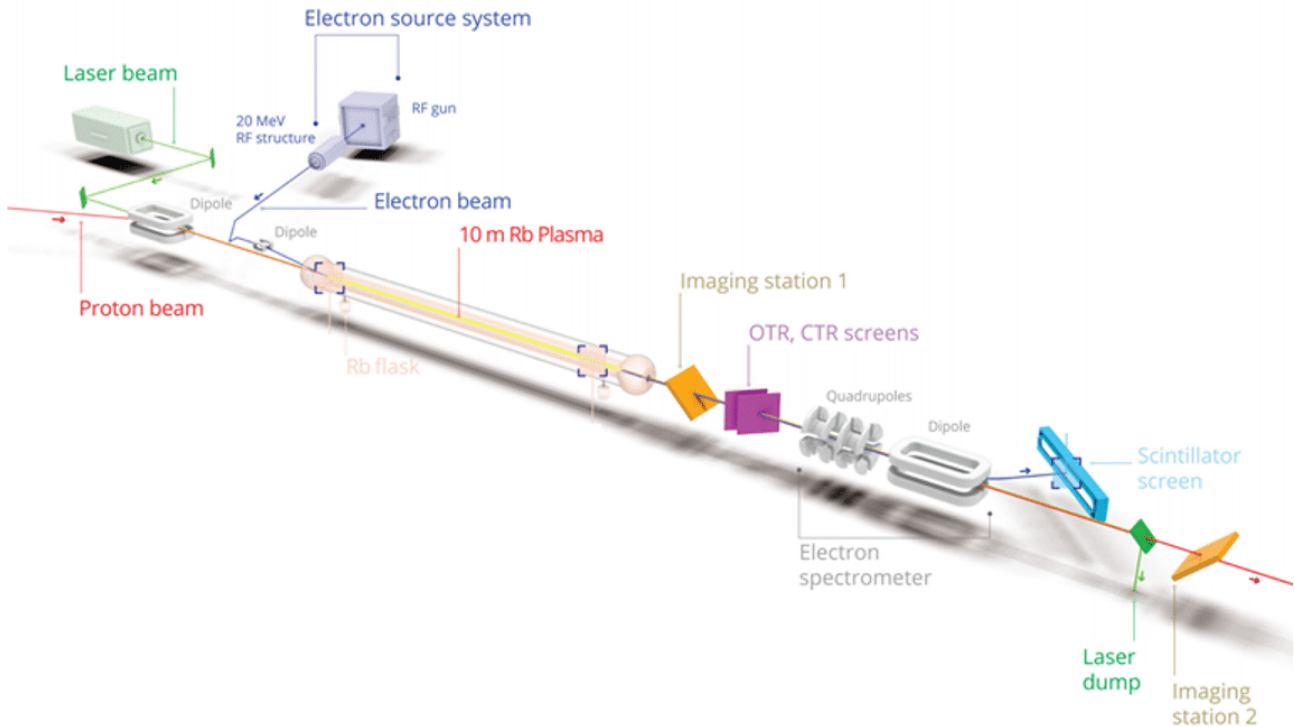
Figure 3: Schematic of the experimental setup of the AWAKE experiment.

3   Experimental Setup

3.1   AWAKE: Beams and Diagnostics

The schematic of the AWAKE experiment is shown in Fig. 3. The main component of the setup is the rubidium plasma source. It is a 10 m long chamber filled with rubidium gas. It is surrounded by a heating setup, such that the density of the gas can be changed. There are ten viewports on each side of the plasma source, placed 0.5 m apart. On each of the viewports there is either a camera or a collimator coupling light to a photomultiplier tube. They are used for observing the amplitude plasma light emitted.

Since AWAKE is a proton-driven plasma accelerator it has a proton beamline (shown in red on the left) coming from the Super Proton Synchrotron. The proton beam is bent towards the common beamline by a dipole magnet and injected into the plasma. Depending on the RIF value (see 2.6.3), the laser pulse is either sent before or after the longitudinal centre of the proton bunch. The electrons are then accelerated by an RF system to around 19 MeV [35], and injected into the plasma with a delay with respect to the RIF. This is done to make sure the wakefields develop enough to have a high amplitude, so the electron energy gain is maximised. Two quadrupole magnets are placed downstream to focus the electron beam. They are then deflected by a dipole onto a scintillator screen. Their energy is then calculated based on their horizontal position on the screen.
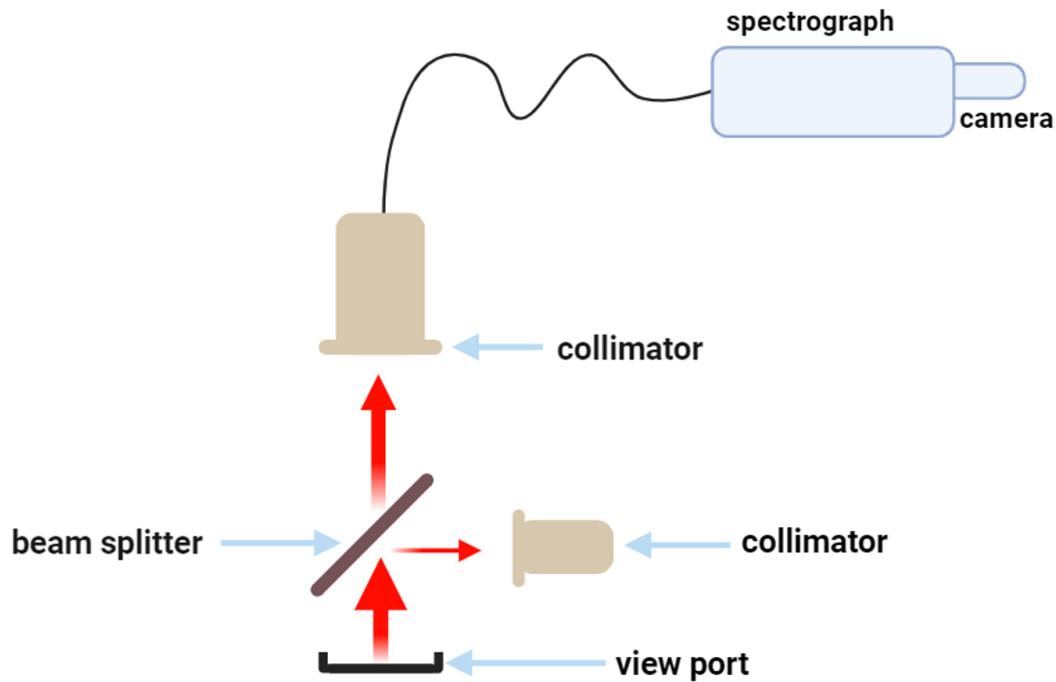
Figure 4: Schematic diagram of the setup used to observe the emitted plasma light spectrum. The components are labelled. Schematic not to scale. The length of the fibre patch cable is 40 m.

3.2   Plasma Light Spectrograph

The spectrograph was first placed on viewport 7/10, 6.5 m along the plasma, since the objective was to observe the light where wakefields were already well-developed. It was then changed to viewport 1/10, 0.5 m into the plasma, since the other objective relied on observing wakefields that were in the beginning stages of their growth. The experimental setup for the observation of the plasma light spectrum is shown in Fig. 4. A photo of it is shown in the appendix. The plasma light exited the plasma source through a viewport and passed through a 8R/92T (8% reflection, 92% transmission) light beam splitter. The reflected light was collected for a different diagnostic. The transmitted light was collimated and sent to a spectrograph using multi-mode fibre optic patch cables. The spectrum was then recorded by a CCD camera. One limitation of the setup comes from the equipment used. The patch cables can only transmit wavelengths between 400 nm and 2200 nm, while the spectrograph can observe wavelengths between 190 nm and 1000 nm, and its efficiency was the highest at around 700 nm. The efficiency curves for the CCD and spectrograph grating are shown in the appendix, in Fig. 19 and 20. This meant that only a part of the entire spectrum could be observed, and that wavelengths further away from 700 nm were detected with lower efficiency, giving the appearance of being weaker.

3.2.1   Spectrograph calibration

The spectrograph used in the diagnostics is the Andor Technology Shamrock SR500i. It has a variable (remotely controllable) slit size and three different gratings with 150 lines/mm, 1200 lines/mm or 2400 lines/mm. The manufacturer reports wavelength ranges of $\approx$ 232.4 nm, 23.5 nm and 0.59 nm for each grating respectively. The first grating was chosen since the number of lines observed was

deemed more important than the resolution. This decision was made by looking at an Atomic Spectra Database created by NIST and finding the most intense lines of rubidium.

To calibrate the spectrograph, pictures of the spectra of argon and krypton lamps were taken, using Oriel spectral lamps. The typical spectra of the lamps as given by the manufacturer are shown in the appendix, Fig. 21 and Fig. 22 in the appendix. At least 20 images of each spectrum were taken, at a few different slit width settings. This was done to see the spectral line width and compare the manufacturer-stated resolution to actual resolution. The spectra obtained are shown in Fig. 23a and Fig. 23b. Those spectra were compared to the manufacturer spectra, and the pixel number was plotted against the wavelength. The line of best fit was plotted through the data, which is shown in Fig. 5. The line shown has the equation $\lambda = 0.114 \times px + (\text{lower bound} + 3.77 \text{ nm})$. This means the spectrum was shifted by almost 4nm, and the actual range that can be measured is ≈ 117 nm, not the 232.4 nm specified by the manufacturer. As will be discussed in section 5.2.1, some of the lines (in both ranges) were close enough together that a 4nm offset would have affected the measured results.

3.2.2   Method of Analysis

The plasma light spectrum is imaged onto a CCD of a digital camera. The CCD is a 1024x1024 pixel array. The data recorded was a 301x1024 ROI of the full array. This was chosen to include the area with the signal and decrease the amount of data that needs to be processed. The image from the camera was smoothed using a median filter to reduce the amount of noise in the image, produced by secondary particles traversing the optical fibre or the CCD. The median filter takes the median of n surrounding pixels and sets the pixel value to that median, where n is the size of the filter. The an example of an image from the camera can be seen in Fig. 6.

Figure 5: Line of best fit made using the obtained calibration spectra and expected spectra.

To find the peak intensity of the spectral lines, the vertical region of interest was chosen by summing the intensity of the pixels along the x-axis and choosing the ROI from the resulting curve. This region was determined to be between 110 and 260 pixel number on the vertical axis. After that, the sum of each vertical slice of the image in the ROI was taken to obtain the light spectrum. The background intensity is then calculated by taking the average intensity of a region of the image without signal. This is then subtracted from the projection, to obtain a background-subtracted spectrum, which can be seen in the appendix, in Fig. 24. To find the intensities of the specific peaks, the locations of those peaks were determined from an image taken at the beginning of the data collection. The area under the peak in the given range was calculated, which gives the final intensity of the given peak.

Since the background was observed to be flat, with no structured noise, the mean value of background intensity could be subtracted from the measurement. Another noise issue was hot pixels, coming from scattered radiation from the beamline. This was unavoidable, as the spectrograph and CCD had to be placed near the plasma setup, as transmitting the signal through many patch cables would lead to
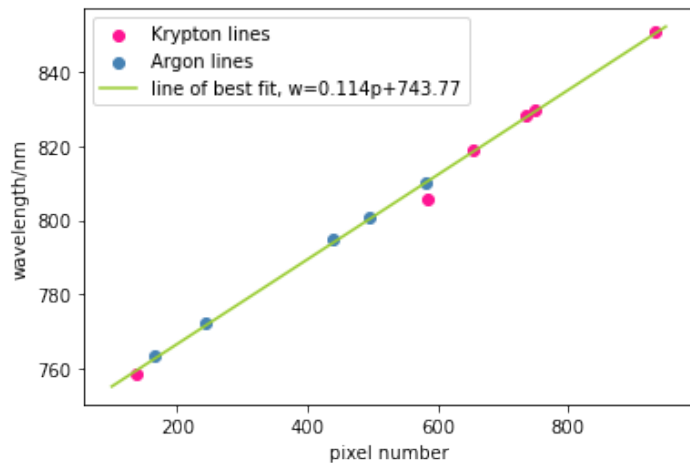
lines [nm]	30m patch cable	5m patch cable	grating efficiency	CCD efficiency	total
424	50.1%	70.8%	60%	10.8%	2.29%
457	53.7%	84.1%	65%	15.1%	4.43%
477	61.7%	89.1%	70%	17.4%	6.70%
780	95.2%	99.3%	57.9%	22.9%	12.56%
794	96.6%	99.3%	56.5%	21.9%	11.89%

Table 1: Efficiency contributions from different parts of the signal transmission setup. The contributions differ for IR and blue ranges. The 5m patch cable was included in the setup twice.

signal loss and deterioration. However, the distance was maximised and the area with the camera was shielded from the radiation by a concrete wall. The effect of the hot pixels on the signal was evaluated by calculating the probability of them affecting the signal, based on the frequency they occurred with and their intensity. It was found that the hot pixels contribute ≈ 1.5 counts per pixel. This was negligible compared to the background noise, which had the average value of ≈ 50 counts per pixel.
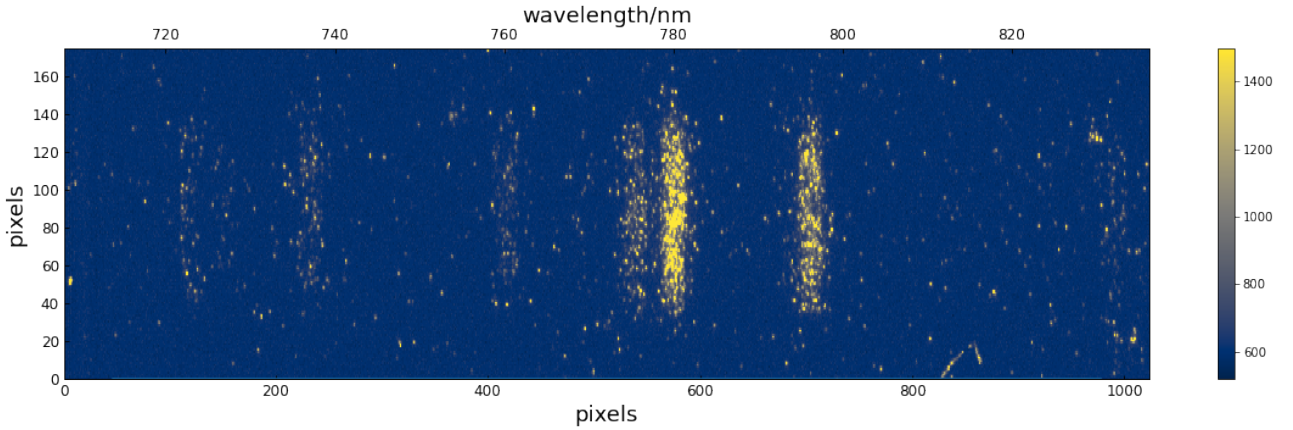

Figure 6: An example of image from the camera.

Since the measurements were taken in the 400 nm-516 nm and 710 nm-826 nm range, there are significant differences between the transmission of these wavelengths of light. Since the goal of the experiment is to determine the intensity ratios between the blue and IR lines, a correction had to be applied to account for the differences. The individual efficiency contributions can be seen in Table 1 In addition to the factors in Table 1, there is also an area correction. The measurements of blue lines were taken with a 350 μm slit size, while the IR lines were taken with a 250 μm slit. This means the width of the lines observed was different, which was accounted for in calculating the correction factor between IR and blue lines. However, all of the factors that were considered are not guaranteed to give a completely accurate difference of intensities due to methods and equipment, as there is an unknown factor coming from the sapphire glass at the viewport and the blazing of the grating.

4 Physics

4.1 Research Question

How do the theoretical predictions for wakefield amplitude at at a small propagation distance into the plasma agree with experimental observations?

4.2 Methods

The investigation into the evolution of the wakefields was done in two ways. First, the plasma light spectrum was measured for different experimental parameters. Second, analytical linear wakefield theory equations were integrated numerically using the same experimental parameters as input. Parts of the derivation of the linear wakefield theory equations are shown to highlight the approximations used in obtaining the theoretical values, not to derive the equations themselves since that is significantly beyond the scope of this thesis. Numerical calculations were made based on those equations to see how changing the position of the bunch with respect to the laser pulse (RIF) changes the wakefield amplitude. The calculations were then compared to the experimental measurements to determine if plasma light measurements follow trends predicted by calculations, and therefore accurately describe wakefield amplitudes.

4.3 Linear Theory Equations

The linear theory is a mathematical model used to describe the behaviour of wakefields analytically. The model is based on the assumption that the wakefield at a certain point in the plasma is a linear sum of the wakefields at all points before it. For AWAKE, this assumption is only correct for short propagation distances into the plasma, before the proton bunch distribution evolves due to self-modulation, as explained in section 2.6.2. Once the bunch has evolved, its shape becomes different and continuously evolves.

The linear theory is derived from the non-relativistic model for the plasma. It can be derived a few different ways [14, 36]. Here the derivation is based on the one shown by C. O'Connell [37], with additional steps and explanation.

The unperturbed plasma will have some density n_{pe} and velocity v_{pe}. When the wakefields are created the density will change such that it will be $n = n_{pe} + \delta n$, where δn is the perturbed plasma density. Similar argument can be made about the velocity, where $v = v_{pe} + \delta v$, where δv is the perturbed plasma velocity. The wakefields can be derived from the linearised equation of motion, continuity equation and Maxwell's equations.

$$\frac{d\mathbf{v}}{dt} = -\frac{e\mathbf{E}}{m} \tag{20}$$

$$\frac{\partial n}{\partial t} + \nabla \cdot n\mathbf{v} = 0 \tag{21}$$

$$\nabla \cdot \mathbf{E} = -4\pi en \tag{22}$$

$$\nabla \times \mathbf{E} = -\frac{1}{c}\frac{\partial \mathbf{B}}{\partial t} \tag{23}$$

$$\nabla \times \mathbf{B} = \frac{4\pi}{c}\mathbf{j} + \frac{1}{c}\frac{\partial \mathbf{E}}{\partial t} \tag{24}$$

Assuming the plasma velocity v_p is small compared to the perturbed velocity and that the unperturbed density n_p of the plasma is a constant, Eq. 20 and 21 can reduce to

$$\frac{\partial \delta \mathbf{v}}{\partial t} = -\frac{e\mathbf{E}}{m} \tag{25}$$

$$\frac{\partial \delta n}{\partial t} + n_p \nabla \cdot \mathbf{v} = 0 \tag{26}$$

Additionally, the equations can be expressed in the coordinate system of the bunch, defined as $\xi = z - v_b t$, which can be written as $\xi = z - ct$ if the bunch is relativistic, which is a valid assumption here (see 2.3). This means equations 25 and 26 can be rewritten in terms of ξ, such that

$$-\frac{\partial \delta \mathbf{v}}{\partial \xi} = -\frac{e\mathbf{E}}{mc} \tag{27}$$

$$-\frac{\partial \delta n}{\partial \xi} + \frac{1}{c} n_p \nabla \cdot \mathbf{v} = 0 \tag{28}$$

Equation 27 and 28 can be combined with the use of $-c\frac{\partial t}{\partial \xi} = 1$ to find

$$c^2 \frac{\partial^2 \delta n}{\partial \xi^2} - cn_p \nabla \cdot \left(\frac{e\mathbf{E}}{mc}\right) = 0 \tag{29}$$

which can again be combined with Eq.22 to find

$$c^2 \frac{\partial^2 \delta n}{\partial \xi^2} + 4\pi n_p (n_p + \delta n)\frac{e^2}{m} = 0 \tag{30}$$

This is a simple harmonic oscillator with the function

$$\frac{\partial^2 \delta n}{\partial \xi^2} + \frac{\omega_{pe}^2}{c^2}\delta n = -\frac{\omega_{pe}^2}{c^2}n_p \tag{31}$$

where ω_{pe} is the plasma electron frequency. It can be replaced by $\omega_p^2 = k_p^2 c^2$, such that the final equation is

$$\partial_\xi^2 \delta n + k_p^2 \delta n = -k_p^2 n_p \tag{32}$$

This was derived for a negatively charged (electron) beam. If the beam is positively charged the RHS of Eq. 32 is $+k_p^2 n_p$ instead [14].

This derivation shows that as long as the linear theory assumptions are correct, the electrons in the plasma will oscillate with with some frequency dependent on the plasma electron density. The solution to this equation can be substituted back into Maxwell's equations to find the equations that describe the amplitude of the wakefields. These equations are taken directly from [14] and are as shown below:

$$W_z(\xi, r) = \frac{e}{\varepsilon_0} \int_{-\infty}^{\xi} n_{b\|}(\xi')\cos[k_{pe}(\xi - \xi')]\mathrm{d}\xi' \cdot R(r) \tag{33}$$

$$W_r(\xi, r) = \frac{e}{\varepsilon_0 k_{pe}} \int_{-\infty}^{\xi} n_{b\|}(\xi')\sin[k_{pe}(\xi - \xi')]\mathrm{d}\xi' \cdot \frac{\mathrm{d}R(r)}{\mathrm{d}r} \tag{34}$$

where W is the wakefield amplitude along the specified direction, k_{pe} is the plasma electron wavevector and $R(r)$ is the transverse dependency given by

$$R(r) = k_{pe}^2 K_0(k_{pe}r)\int_0^r r\mathrm{d}r' n_{b\perp}(\xi')I_0(k_{pe}r') + k_{pe}^2 I_0(k_{pe}r)\int_r^\infty r\mathrm{d}r' n_{b\perp}(\xi')K_0(k_{pe}r') \tag{35}$$

where $n_{b\perp}$ and $n_{b\|}$ are functions describing the transverse and longitudinal profiles of the drive bunch, and I_0 and K_0 are zeroth order modified Bessel functions of first and second kind.

4.4 Results

4.4.1 Calculation of Wakefield Amplitudes

The code used for the numerical integration of the equations is given in the appendix. It includes a function for the calculation of $R(r)$ for a given r, and a calculation for $\frac{dR(r)}{dr}$. The optimal r was determined from plotting the curve of $R(r)$ and finding the maximum, as that would maximise $W_z(\xi, r)$. This r was found to be approximately $1.3\sigma_r$. The code was written such that by changing the longitudinal position of the centre of the bunch the RIF position can be changed. This makes it possible to observe the changes in wakefield amplitude. Additional code (not shown here due to low complexity) was then written to display the wakefield amplitudes and compare the focusing and defocusing field.

A summary of the calculation results is shown in Fig. 7. The LHS of the figure shows the change in longitudinal wakefield amplitude as the RIF position is changed and the RHS shows the same for radial wakefields. The presence of plasma is indicated by the shaded orange region. The wakefields are shown in blue, and the longitudinal profile of the proton bunch is shown in pink. As mentioned before, when the bunch is perfectly Gaussian and in the plasma (see Fig. 7, bottom LHS) there will be very small resulting longitudinal wakefields induced. There, the bunch passes through the plasma a significant amount of time after it is created, therefore all contributions from individual protons in the bunch cancel each other out, resulting in no longitudinal wakefields. As the RIF position gets closer to zero (i.e. the centre of the longitudinal bunch profile), the amplitude of the wakefields increases, reaching a maximum at RIF = 0 (4th row in Fig.7). The simulations corresponding to the RHS of the plot result in a transverse wakefield amplitude distribution shown in Fig. 8a. An additional simulation with noise added to the bunch profile was also completed, which results in an analogous plot. This plot is shown in Fig. 8b. The noise added was random noise of $\pm 1\%$ of the height of the Gaussian. These calculations were performed to demonstrate the effect of imperfections in the bunch. It can be seen that at some values of RIF position (Fig. 8b) there are sudden peaks in the maximum transverse wakefield amplitude, caused by the noise.

4.4.2 Plasma Light Spectrum Measurements

The setup used for plasma light spectral measurements is shown in Fig. 4. It uses the exact same equipment as used for the Applied Physics section (see Sec. 3.2), except for the position of it was changed from viewport 7, located 6.5m downstream of the plasma entrance, to viewport 1, 0.5m downstream of the plasma entrance. This was chosen since it gave the best chance of demonstrating the behaviour that was calculated, which assumes no bunch evolution. The measured amount of plasma light for different spectral lines during a RIF timing scan are shown in Fig. 9. This intensity is also plotted against the simulated intensity in Fig. 10 to show the agreement in the shape of data between the measurement and calculation. The maxima of the plots do not correspond to each other, so this plot cannot give quantitative information about the conversion between transverse wakefield amplitude and plasma light intensity, and is meant to show the shapes of the graphs are very similar.

The "test" line was added to show the increase in intensity of the 780 nm and 794 nm lines is due to increased signal, and not incidental. If it was, the test line would increase as well, but it can be seen that it does not, and it is at the level of background intensity. The error bars show the standard deviation of the intensities that were observed for each RIF position. The RIF positions (horizontal axis) are assumed to have no error, as they can be set with picosecond precision, and could not be seen on the scale of ≈ 100 ps.
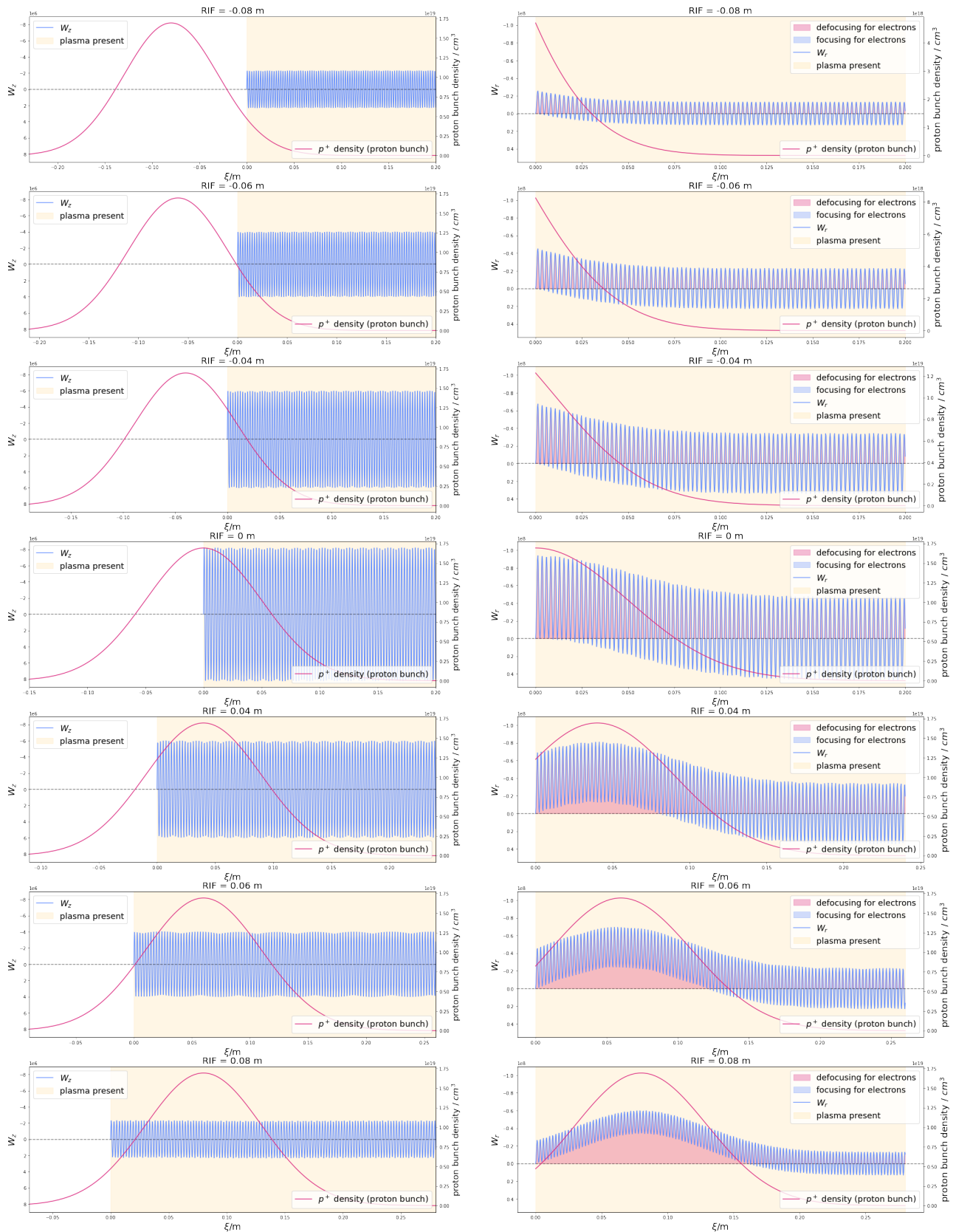
Figure 7: Calculated wakefield amplitude as a function of the RIF position. The left plots show the amplitude of the longitudinal wakefields, right plots show the transverse wakefields as a function of ξ (position along the bunch). The shaded orange area on the plots shows where plasma is present. On the RHS plots the shaded blue area is a focusing field, and the red area is a defocusing field. The proton bunch is marked in pink.
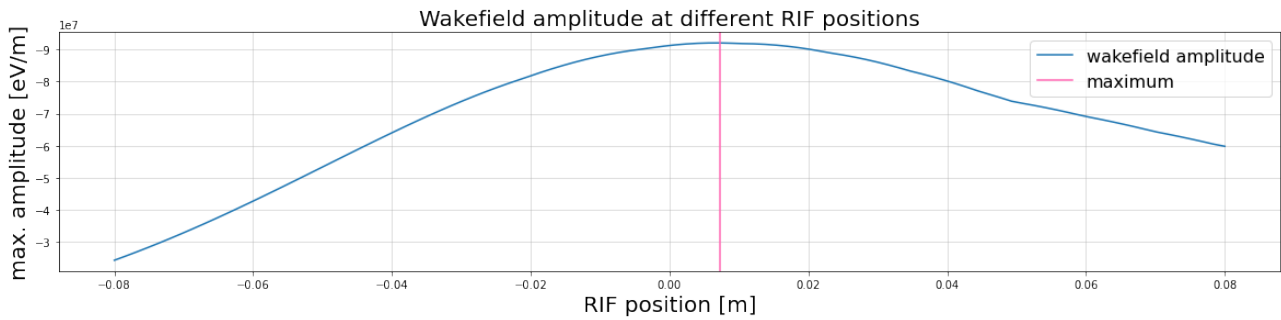
(a) Graph of simulated wakefield amplitudes for different RIF positions.
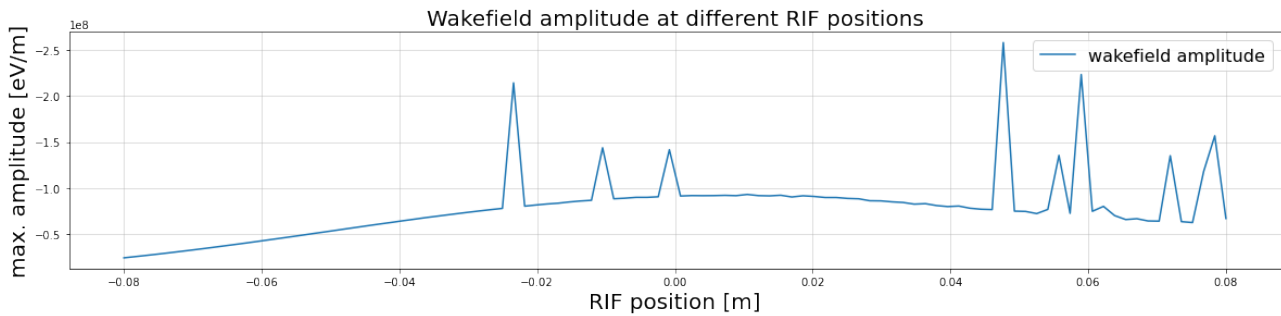
(b) Simulated wakefield amplitudes for different RIF positions with random imperfections of amplitude $\pm 1\%$ added to the drive bunch. The extreme RIF positions now show extreme variance in wakefield amplitude.

Figure 8: Figures showing the wakefield amplitude with relation to the RIF position.

4.5   Discussion

The wakefield amplitudes were calculated by using the linear wakefield equations and a Gaussian longitudinal proton bunch profile. The assumption of a longitudinally Gaussian bunch profile is only valid at very small propagation distances into the plasma ($z \approx 0$m). The equations were used to evaluate the wakefield amplitude at different RIF positions, and they show that the highest wakefield amplitude occurs close to when the seed wakefield amplitude is the largest (RIF = 0.01 m).

This was compared to an experimental observation of plasma light intensity compared to RIF timing. This was done 0.5 m into the plasma, which was the smallest distance possible, to minimise bunch evolution. However, in the experimental results it can be seen that the maximum light intensity occurs at RIF ≈ 0.05m. This corresponds to a position where the bunch population in the plasma is larger, but the seed wakefield amplitude is smaller. This could indicate that at 0.5 m into the plasma the wakefield amplitude no longer follows that calculated from linear regime equations. However, Fig. 10 shows that the growth of the wakefields and light amplitude is very similar, despite the maximum of the curves being shifted.

It can be seen that measurements have very large uncertainty values. This can be understood by looking at the image shown in Fig. 6 in section 3.2.2. The signal level was often very low due to the small viewport, low transmission efficiency of the setup, and very rapid decay time of the plasma (order of microseconds). This either contributed to the low amount of light that could be collimated and detected, or further signal degradation during transmission. This meant that the signal amplitude could vary by a large fraction between measurements. Attempts to reduce this effect were made by making the ROI the signal was integrated over as large as reasonable without significantly increasing the amount of noise included, due to hot pixels or stray proton radiation. Additionally, this data was only taken for IR lines, not blue lines. It is possible the blue lines show different behaviour from the

IR ones, as can be seen in Section 5.3.

Lastly, it is not certain where the IR light comes from. Since those wavelengths correspond to recombination light, it could come from either the electrons that were excited by the laser exciting rubidium atoms outside the plasma, which then recombined, or from the plasma recombining after the laser and wakefields were gone. Due to that, this problem is exclusive to IR lines, as the blue lines can only be observed when the rubidium is ionised, ie. when plasma exists. This was not possible to measure with the spectrograph in the current setup, as the signal-to-noise level would not allow for time-resolved spectrum measurements. This means that future measurements could be done to determine when this light is observed. This could be accomplished by triggering the acquisition of a spectral image after the wakefields are gone or by using a PMT with a notch filter placed on it. This would give more information about the time evolution of the spectra, as the PMT could detect signals of much lower amplitude, and a notch filter would only allow the desired lines to pass through. This measurement would give an indication of the relevance of IR light for determining wakefield amplitude. Additionally, since this problem is exclusive to IR lines, the blue lines could be studied before, sd they can only exist while the wakefields are present. Due to that, they could be a more applicable diagnostic.
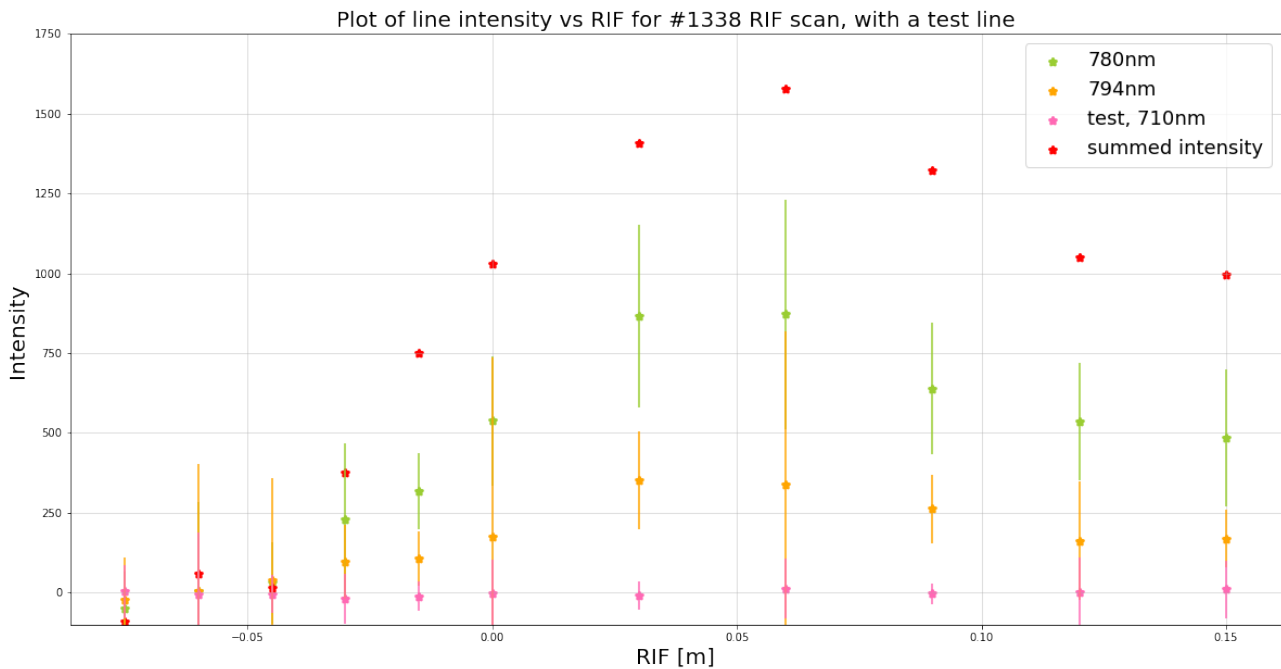

Figure 9: Intensity of IR plasma light as a function of RIF position. The contributions of the two strongest lines are shown (in orange and green), in addition to the summed intensity (in red) and a test line at no signal (pink). The summed intensity is shown with no error, since it covers the individual measurements.
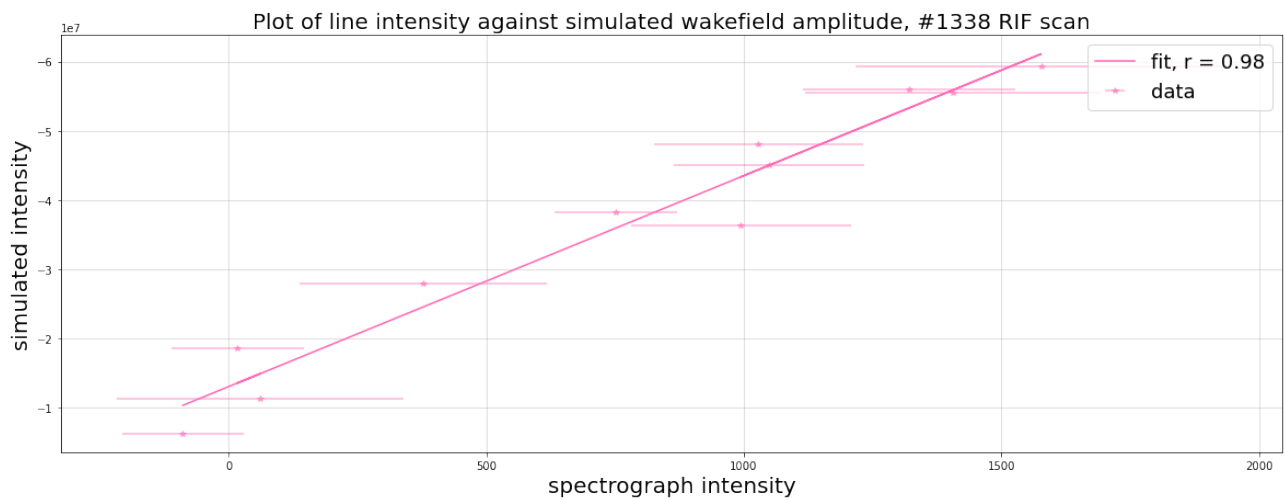
Figure 10: Intensity of IR plasma light plotted against simulated wakefield amplitude. A line of best fit was plotted through the data

5   Applied Physics

5.1   Research Question

The intensity of light emitted by the plasma has been shown to be proportional to the energy loss of the drive bunch (in some cases). This can happen due to two mechanisms:

- The drive bunch delivers energy to the electrons. They quickly reach thermal equilibrium with their surroundings (ions), which results in an increased electron and ion temperature. This means the amount of light emitted will increase as well.

- The drive bunch delivers energy to the electrons. They lose their energy incrementally, through collisions with the ions, exciting other electrons. This causes an increase in the amount of emitted light.

Both of the hypotheses lead to an increase in emitted light, but the rate of the increase and the ratio of increases can lead to information as to which of the hypotheses is correct, as can be seen from section 2.5, where it was said that the intensity of lines will depend on the temperature. The research question is therefore: **How do ratios between different spectral lines of rubidium evolve with changing seed wakefield amplitude? What can be inferred about the temperature of the plasma electrons and the mechanism through which they lose energy?**

5.2   Methods

5.2.1   Analysis of Measured Rubidium Spectral Lines

All rubidium spectral lines were observed at the beginning of data collection. This was done by taking multiple measurements of different wavelength ranges in 100 nm increments and stitching it together using Python. The exact method of data analysis was described in section 3.2.2. The full spectrum can be seen in Fig. 11, broken up into two spectra for better visibility. The full summary of all lines that were visible is shown in the appendix.

From this image it was determined that the most useful ranges that could be taken were 400 nm-516 nm (referred to as the "blue range") due to the concentration of lines, and 710 nm-826 nm (referred to as "IR range") due to them being the strongest lines. In those ranges, the IR lines are all Rb I lines, which come from unionised rubidium [38]. The lines in the blue range are all Rb II lines, from singly ionised Rb.

It was confirmed that these lines are Rb II lines by looking at the spectrum during a laser energy scan, a measurement where the line intensities are measured at a range of laser energies. When only the laser beam is present the electron temperature is expected to be low, approximately 0.5 eV [39], which means it is very unlikely (essentially not possible) for these lines to be visible. During that scan none of these lines were visible, which confirmed the lines were indeed Rb II lines. The summary of the used lines including their wavelength obtained from calibration, the wavelength from the NIST Atomic Spectra Database, and the atomic transitions corresponding to these lines are given in table 4 and 5 in the appendix. The lines appear very wide due to the large slit width setting of the spectrograph, needed for the signals to be observable at all. This causes a slight problem around the 425 nm mark, where the 424 nm and 427 nm lines occur. Since they are close together, increasing the slit width to increase the signal would cause them to become unresolvable. However, decreasing the signal decreases the signal to noise ratio, reducing data quality.
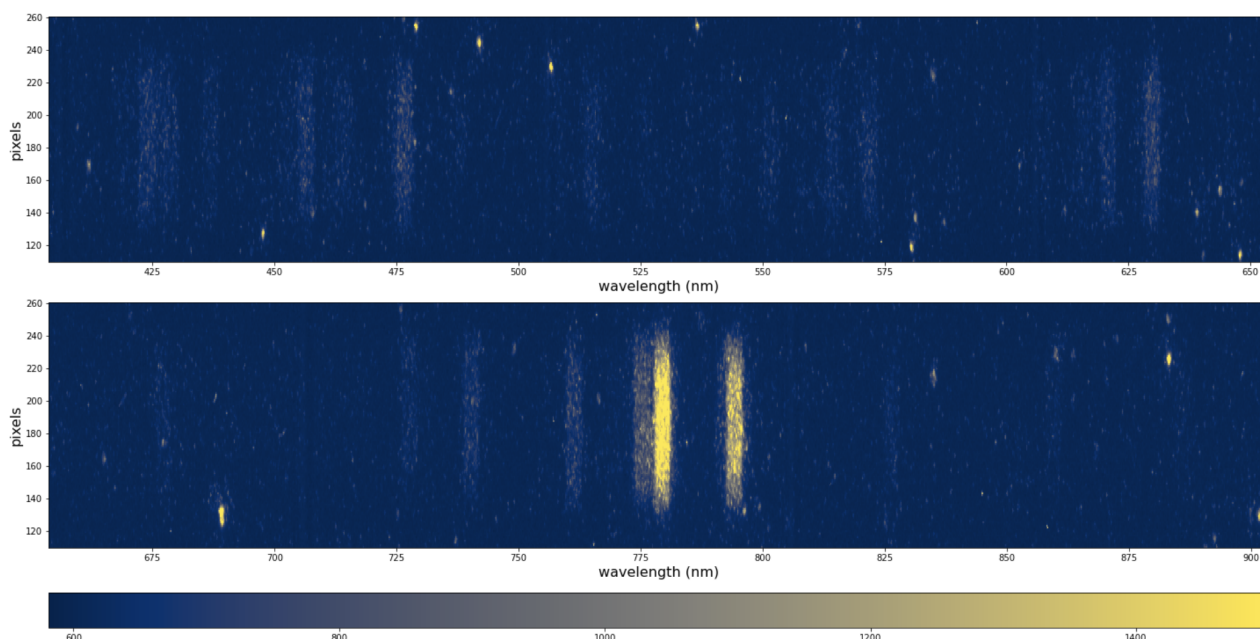
Figure 11: Stitched image of the entire measurable rubidium spectrum. It was broken up at 650 nm to improve readability.

5.2.2   Analysis of Lines from NIST database

The NIST Atomic Spectra Database is the main source of information about spectral lines of atoms and the changes in their intensity based on the gas density and electron temperature. The NIST data was analysed before taking experimental data to form an expectation for experimental results. The absolute line intensities for chosen IR and blue lines are shown in Fig. 12a and Fig. 12b.

It can be seen that all the lines exhibit the same behaviour at different rates. All of them have very low initial intensity which increases, after which it plateaus. This is expected, as the occupation probability of the levels scales with temperature as described by Boltzmann's distribution (mentioned in section 2.5) if a local thermal equilibrium is established.

Next, the ratios between the IR and blue lines were plotted, as observing those ratios is expected to be more accurate than observing the absolute intensity. This is due to the fact that an unknown amount of signal is lost due to poor collimation of light, signal loss in the fibres, attenuation in the viewports and many more. The ratios of lines and a fit of a Boltzmann function are shown in Fig.13a and 13b. This result is of interest, as it shows that the ratio between two lines should be constant for IR lines, except at very low temperatures. The same can be observed for the blue lines, but the constant region is reached at a higher temperature for the 424 nm/ 477 nm ratio. Additionally, the IR lines share an energy level and have a very similar frequency, so they are likely to have equal populations.

Lastly, if intensities of the lines are plotted it can be seen that for some values of electron temperature the intensity of IR lines is much higher than that of blue lines. This is visualised in Fig. 14. The 424 nm blue line becomes higher than the 794 nm line at 6 eV and around 8 eV for the 780 nm line. This means that above some temperature most of the observed light comes from the blue range, not the IR range, despite the fact the IR lines are much stronger at lower temperatures. In Fig. 14b it can be seen that below 4 eV most of the light is contributed by the IR lines. Above that they are overtaken by the blue lines, especially the 424 nm line.
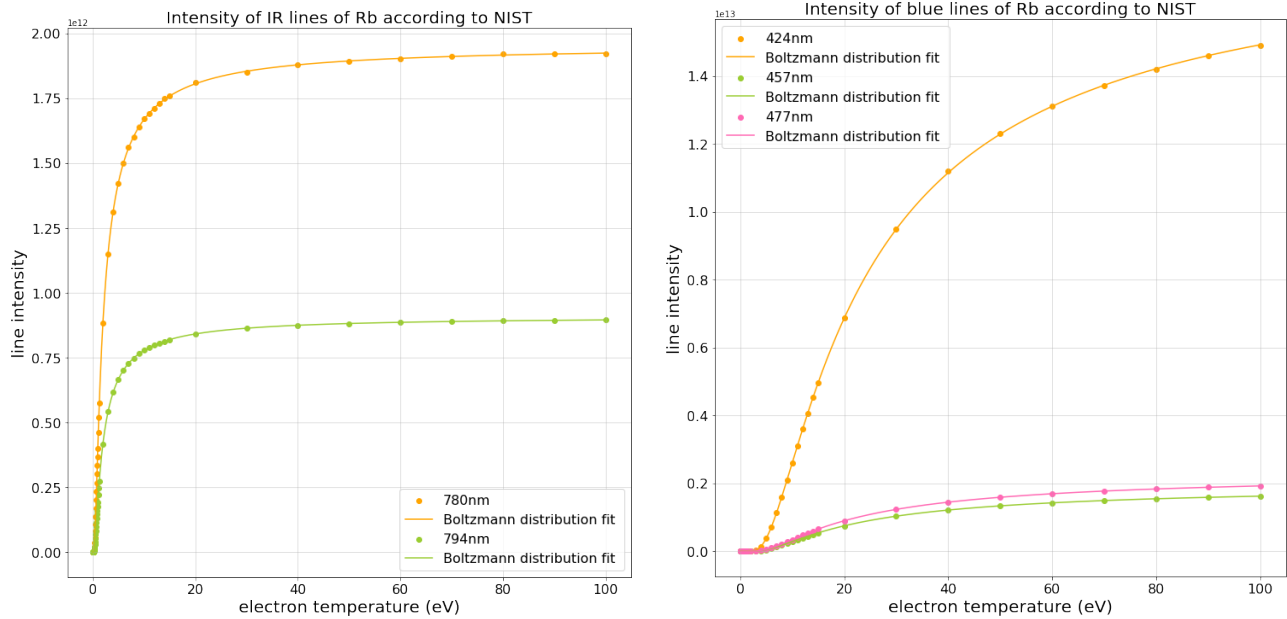
(a) Graph of the intensity of the 780 nm and 794 nm Rb I line.

(b) Graph of the intensity of the 424 nm, 457 nm and 477 nm Rb II line.

Figure 12: Graphs of line intensity vs electron temperature. All of the lines show initially very low intensity, after which it increases and levels out.

5.2.3   Relative Ionisation Front (RIF) Scan

Changing the position of the ionising laser with respect to the proton bunch changes the number of protons in the plasma, and it changes the initial proton bunch amplitude that the plasma "sees", as described in section 2.6.3. As this is expected to first increase and then decrease the amplitude of the wakefields, observing the light that is emitted at various RIF positions could give an indication of the behaviour of the wakefields.

5.3   Results

The RIF position scans were taken for both of the identified plasma light wavelength ranges, for different configurations of proton bunch density and plasma density. The experimental parameters are summarised in Table 2. The results from the first configuration (#1308) are not shown, as the range of RIF positions that was taken for that data set was different than for the rest, which made it difficult to compare it to the rest of the data. For the two remaining data sets (#1317, #1332) the intensity of lines as a function of RIF position and as a plot of intensity of lines against the strongest line observable in that range. These results show a strong linear correlation between the individual line intensities. The ratios between the lines that can be inferred from these graphs and calculated are shown in Table 3. The values were based on equations 14 and 15. They show good agreement for the IR lines, but very poor agreement for the blue ones.

In graphs 15a and 16a, results suggest that the IR lines reach their highest intensity (saturation value) for values of RIF > 0 m, while blue lines may keep increasing.

A graph combining the data from RIF scan #1317 and #1332 is shown in Fig.17. It shows the intensity of different spectral lines at different RIF positions. This data was not taken in a single scan, as can be seen by the red and blue points not aligning. This was caused by limitations of the setup, but was
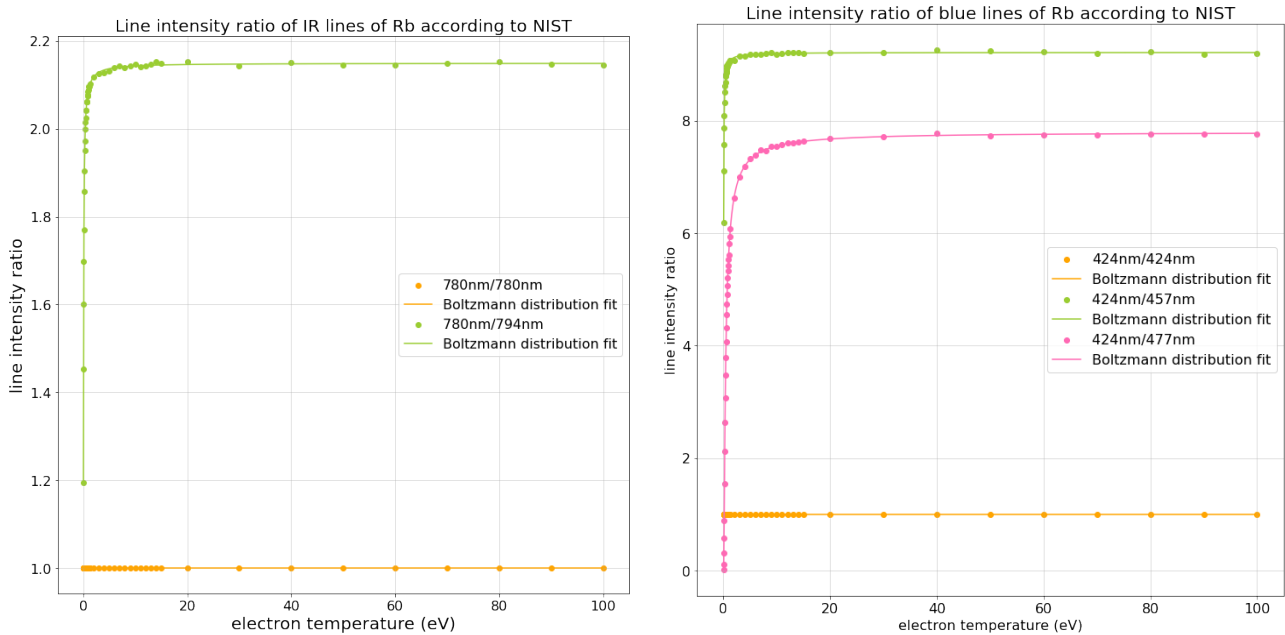
(a) Graph of the intensity of the 780 nm and 794 nm Rb I line with respect to the 780 nm line.

(b) Graph of the intensity of the 424 nm, 457 nm and 477 nm Rb II line with respect to the 424 nm line.

Figure 13: Graphs of line intensity ratio vs electron temperature.

event code	bunch density	plasma density	range	figure
#1308	3e11	3.8e14	400nm-516nm	
#1317	3e11	7.4e14	400nm-516nm	Fig.16
#1332	3e11	2e14	710nm-826nm	Fig.15

Table 2: Summary of the experimental measurements taken for determining the temperature of plasma and behaviour of spectral lines.

determined to not have a large impact on the amplitudes of the lines. This was evaluated by comparing the intensity of the events from event #1308 and #1317, since they were taken for the same range, with the same bunch population, but at different plasma densities. The graph was corrected for the transmission efficiency of the setup, as the raw measurements indicate a much lower intensity of blue than IR.

5.4   Discussion

From the results it can be seen that the ratio of the spectral lines seems to be constant for most of the measurement, with a high accuracy of the fit despite the large uncertainty. This could mean that the assumption about the relative populations of the lines being close enough and that the temperature-dependent term seems to drop out of the relation for intensity of the lines is correct. Otherwise said, the difference in energy between the two transitions is small enough it can be neglected with respect to the temperature of the electrons. That considered, the large difference between the calculated ratio between intensities and the measured one indicates this might not be true. This is additionally supported by the fact that the population of the 424 nm transitions increases more than the other blue lines. This could also be due to the fact, that the blue lines are all ion lines, so additional energy is
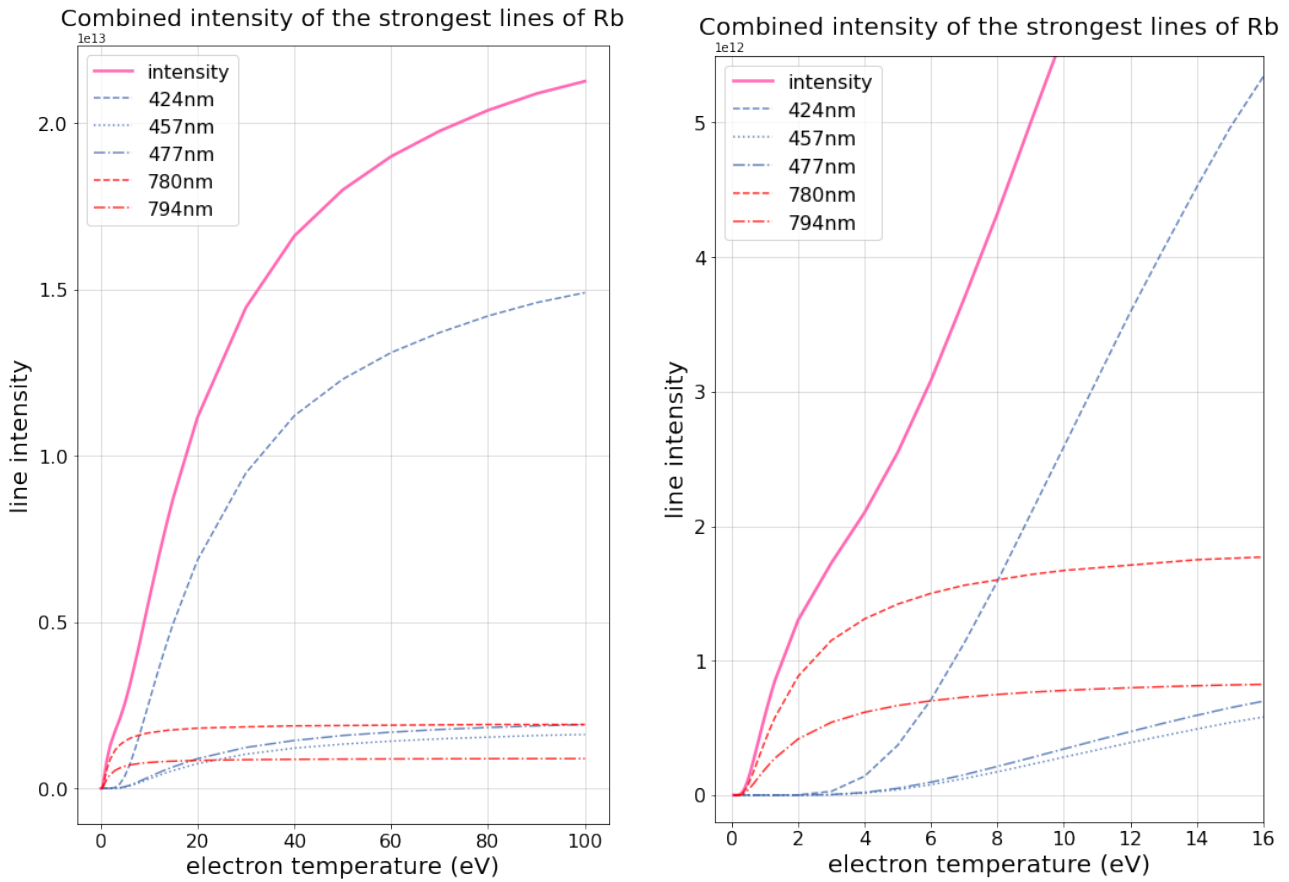
(a) Graph showing the contribution of blue lines to the combined light intensity.

(b) Zoomed-in graph of the region where IR lines contribute the most.

Figure 14: Graph of individual line intensities with respect to electron temperature, compared to the combined line intensity.

required for them to become excited, especially considering Rb is an alkali metal. This means that the first electron is more loosely bound than the second. This could mean the relations described in section 2.5 are only relevant for the Rb lines, not ion lines. This also means that the electron temperature cannot be reliably estimated from these measurements.

For the comparative graph, it can be immediately noticed that the shapes of spectral line intensity curves in Fig. 17 and 14b appear very similar. For the IR lines, both of them show an immediate increase in IR light intensity, followed by plateau. For the blue lines, an initial level of limited growth (very well seen in the 477 nm line in Fig. 17) is followed by a rapid increase.

An important insight these results bring is the realisation about the lack of understanding of electron behaviour in the case of plasma wakefields. When the plasma is at a low temperature, the temperature

	424nm/457nm	424nm/477nm	780nm/794nm
measured	3.5 ± 0.2	1.9 ± 0.2	2.04 ± 0.07
calculated	7.9	6.2	2.07

Table 3: Summary of the experimental results describing the ratios between different spectral lines, compared to the calculated results. The method for calculating the results is described in section 2.5

of the electrons is assumed to be the same as the temperature of ions. It is also assumed that the speed distribution of the electrons is defined by the Boltzmann distribution. The centre of this distribution is defined by the most probable velocity of the electrons. As temperature increases, the most probable velocity increases, and the distribution spreads out. However, it is not known if those electrons follow the Boltzmann distribution when they form wakefields. They gain velocity due to their oscillation, which means they now move much faster than the unperturbed plasma velocity. This means that the Boltzmann distribution either spreads out to reach very high values, or stops being applicable completely. This also matters, as the NIST database assumes the electron and ion temperature remain
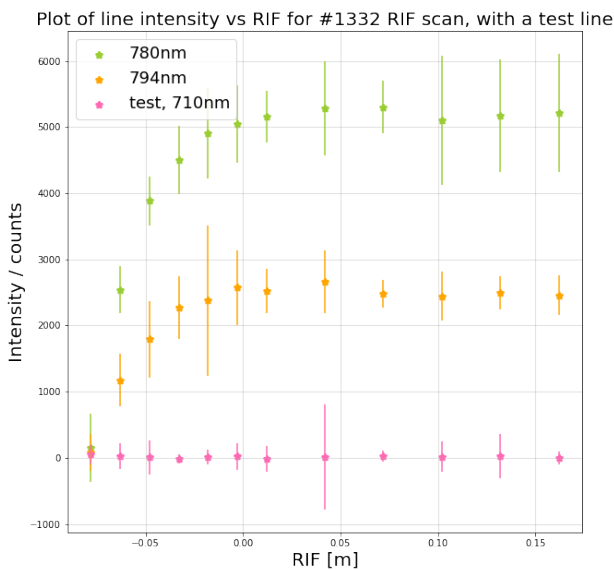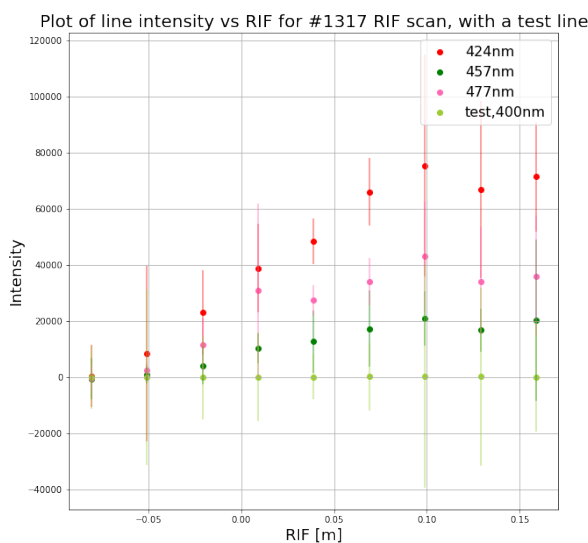

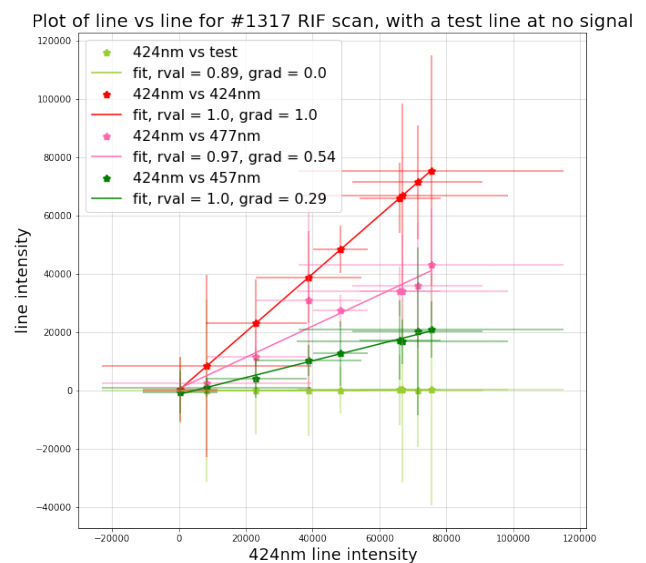(a) Intensity of different IR spectral lines as a function of RIF position.
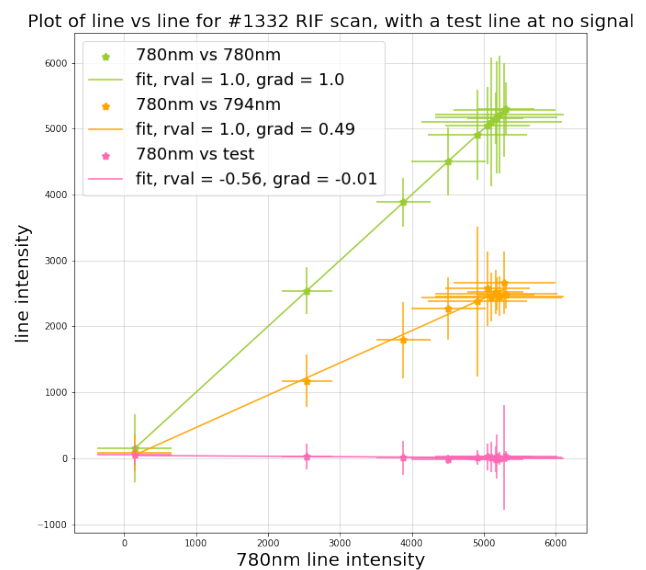
(b) Intensity of different IR spectral lines of Rb plotted against the 780 nm line intensity.

Figure 15: Results of a RIF position scan measurement for the IR range.

(a) Intensity of different spectral lines as a function of RIF position.

(b) Intensity of different blue spectral lines of Rb plotted against the 424 nm line intensity.

Figure 16: Results of a RIF position scan measurement for the blue range.

the same as the temperature increases, which might not be true in this case, where it was assumed the atoms are virtually static. If the time of observation is small enough, it could be assumed the electrons have not reached equilibrium with the ions. This would explain the discrepancy between the ratio between lines expected from the NIST database, and the discrepancy between the ratios calculated from the Boltzmann distribution and transition probabilities. Another issue with the calculation of expected line ratios is the fact that it requires the assumption that the populations are equal (see Sec. 2.5). While this is likely to be valid for the IR lines as mentioned earlier, the same might not be the case for the blue lines, since their energy differences are larger and not all of them share energy levels. Last discrepancy that needs to be addressed is the unexpected behaviour of spectral lines with respect to the wakefield amplitude. As was shown in section 4.4, the amplitude of the wakefields should decrease when the values of chosen RIF position are too large, since the seed wakefield amplitude is decreased. This means the intensity of spectral light observed should decrease as well. The fact that this does not appear to happen could indicate that the relationship between wakefield amplitude and plasma temperature is not a straightforward one. This means this behaviour needs to be studied more, preferably with more sensitive equipment capable of time-resolved images, as explained in section 4.5.
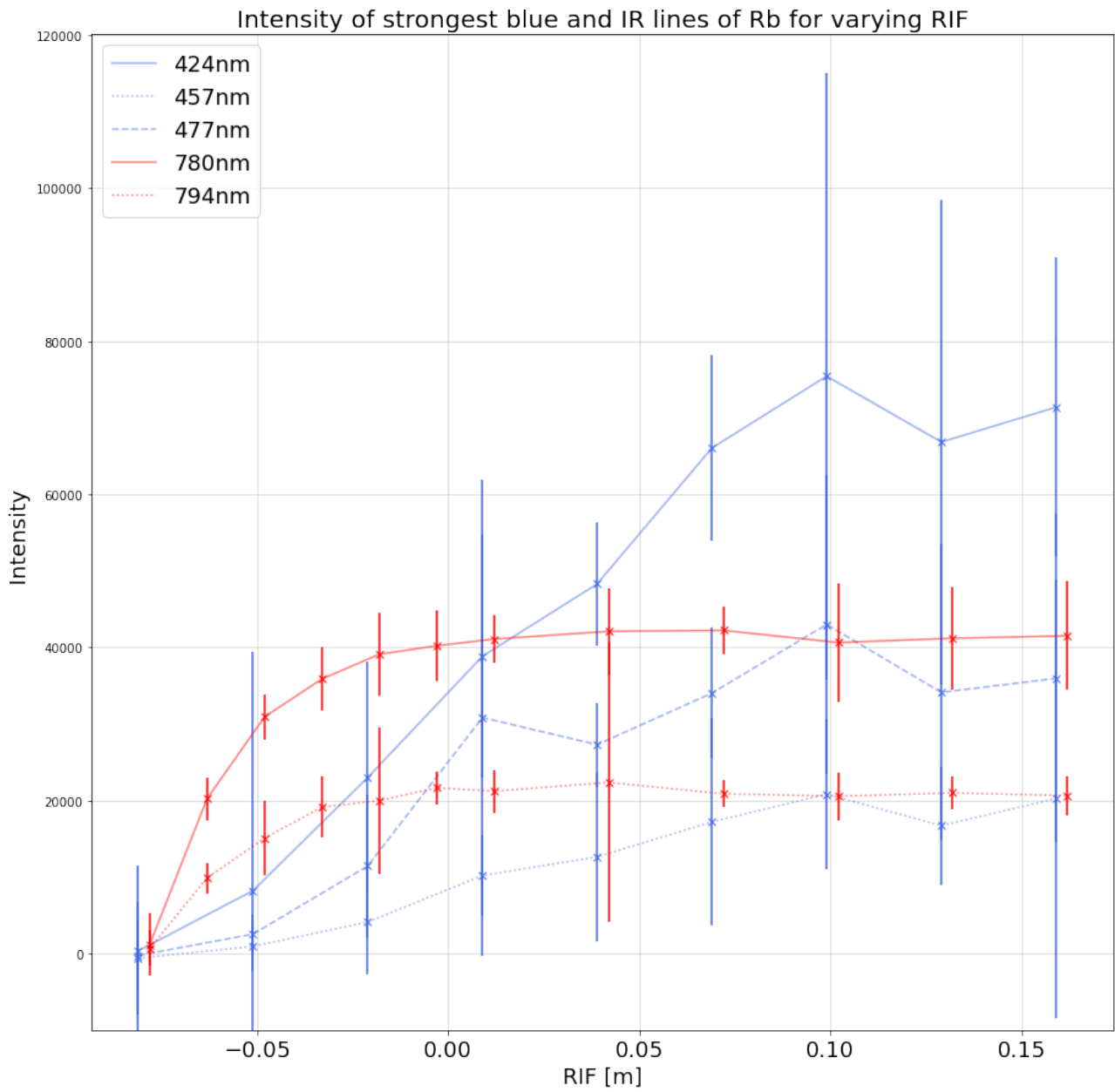
Figure 17: Intensity of strongest blue and IR lines for different RIF positions.

6 Conclusion

This experiment was undertaken to evaluate if measurements of plasma light emitted during wakefield excitation reveal information about excited wakefield amplitude. This was done by looking at theoretical prediction of wakefield amplitude with relation to the bunch population and initial wakefield amplitude. Those results were then compared to experimental observations. The observed agreement is limited, which may be due to the proton bunch having already evolved over the first 0.5 m of plasma (the earliest position along the plasma where the measurement could be taken). However, the growth of the wakefields and plasma light intensity is very similar, which indicates that there is information about the wakefields in the plasma light. Better agreement could be obtained by performing numerical simulations that include bunch evolution due to the self-modulation process or by observing the blue light instead of the IR.

The second part of the experiment included the comparison of the observed light intensities during RIF position measurement to the changes in light intensity with changes in temperature. First, it can be concluded that determining the temperature from these measurements is not possible without knowing the level population, which might not be equal for two lines. Second, the similarities between RIF and temperature vs intensity graphs are very strong, and suggest that the IR line intensity saturates for certain measurements. It also implies there might be a connection between the RIF position and temperature of the plasma, but this cannot be concluded definitely, as a different mechanism could be causing the similarity between the those graphs. This is surprising, but could be explained by inadequacies of the measurement setup for this kind of experiment. First, the integration time of the spectrograph used is very large compared to the duration of the laser pulse, the wakefields and the plasma. This means this kind of measurement may not be suitable to draw conclusions about the wakefield amplitudes. Drawing conclusions about wakefield amplitude from plasma light intensity is only valid when observing singular lines, which do not saturate in intensity. To investigate the validity of individual lines, another set of measurements should be performed by using a PMT or a camera with filters in front of them. This would let specific wavelengths of light to be observed while varying the integration window such that the time when most of the light is emitted can be determined. If most of the light is emitted after the lifetime of the plasma, then all the observed light is not likely to give information about the wakefields, but rather about the plasma itself. Contrary to that, if the majority of the light is emitted when the wakefields are present, the light emitted after that needs to be gated out of the measurements, but the initial light gives information about the fields. This way the new measurement will result in a more accurate picture of the applicability of specific lines for wakefield amplitude estimations.

Bibliography

[1] E. Oz, C. D. Barnes, C. E. Clayton, F. J. Decker, S. Deng, M. J. Hogan, C. Huang, R. Iverson, D. K. Johnson, C. Joshi, T. Katsouleas, P. Krejcik, W. Lu, K. A. Marsh, P. Muggli, C. O'Connell, and D. Walz, "Optical Diagnostics for Plasma Wakefield Accelerators," *AIP Conference Proceedings*, vol. 737, pp. 708–714, 12 2004. https://doi.org/10.1063/1.1842612.

[2] R. Widerøe, "Über ein neues Prinzip zur Herstellung hoher Spannungen," *Arch. Elektrotech.*, vol. 21, pp. 387–406, 1928. https://cds.cern.ch/record/434681, DOI: 10.1007/BF01656341.

[3] L. Yarris, "Invention for the ages." https://www2.lbl.gov/Science-Articles/Archive/early-years.html.

[4] G. Agosta, "The concerns of people living along the route of cern's future collider," Apr 2024. https://www.swissinfo.ch/eng/science/the-concerns-of-people-living-along-the-route-of-cerns-future-collider/76209091.

[5] D. Castelvecchi, "Cern's 17-billion supercollider in question as top funder criticizes cost," *Nature*, vol. 630, p. 539–540, Jun 2024. 10.1038/d41586-024-01671-8.

[6] S. Sermondadaz, "Cern entices authorities over gigantic collider with green arguments," Apr 2023. https://genevasolutions.news/science-tech/cern-entices-authorities-over-gigantic-collider-with-green-arguments.

[7] J. Norem, A. Hassanein, Z. Insepov, and I. Konkashbaev, "Breakdown in rf cavities," *Proceedings of the 2005 Particle Accelerator Conference*, p. 1886–1888, 2005.

[8] E. Oz, C. D. Barnes, C. E. Clayton, F. J. Decker, S. Deng, M. J. Hogan, C. Huang, R. Iverson, D. K. Johnson, C. Joshi, T. Katsouleas, P. Krejcik, W. Lu, K. A. Marsh, P. Muggli, C. O'Connell, and D. Walz, "Optical Diagnostics for Plasma Wakefield Accelerators," *AIP Conference Proceedings*, vol. 737, pp. 708–714, 12 2004.

[9] G. Pert, *Foundations of Plasma Physics for Physicists and Mathematicians*. John Wiley & Sons, Inc, 1 ed., 2021.

[10] P. Gibbon, "Introduction to plasma physics," *Proceedings of the CAS-CERN Accelerator School: Plasma Wake Acceleration*, p. 51–65, 2016. http://dx.doi.org/10.5170/CERN-2016-001.51.

[11] A. Piel, *Plasma Physics*. Springer Science and Business Media, Jun 2010.

[12] F. Chen, *Introduction to Plasma Physics and Controlled Fusion*. Springer Science and Business Media, 2016.

[13] S. Errede, "Lecture notes 18.5," *Lect. Notes*, vol. 18, 2015. https://hep.physics.illinois.edu/home/serrede/P436/Lecture_Notes/P436_Lect_18p5.pdf.

[14] P. Muggli, "Beam-driven, plasma-based particle accelerator," *Proceedings of the 2014 CAS-CERN Accelerator School: Plasma Wake Acceleration*, vol. 1, Feb 2016. https://e-publishing.cern.ch/index.php/CYR/article/view/217.

[15] R. Fitzpatrick, *Plasma Physics: An Introduction*. CRC Press, 2 ed., 2022.

[16] *Proceedings of the 2014 CAS-CERN Accelerator School: Plasma Wake Acceleration*, vol. 1, 2016. `https://doi.org/10.5170/CERN-2016-001`.

[17] Z. Deng and J. H. Eberly, "Multiphoton absorption above ionization threshold by atoms in strong laser fields," *J. Opt. Soc. Am. B*, vol. 2, pp. 486–493, Mar 1985.

[18] D. J. Griffiths and D. F. Schroeter, *Introduction to Quantum Mechanics*. Prentice Hall, 3 ed., 2018.

[19] C. Kittel, *Chapter 6: Free Electron Fermi Gas*, p. 136–137. John Wiley & Sons, 8 ed., 2005.

[20] R. B. Leighton, *10-1: Derivation of the Three Quantum Distribution Laws*, p. 332–341. McGraw-Hill, 1959.

[21] T. Tajima and J. M. Dawson, "Laser electron accelerator," *Physical Review Letters*, vol. 43, p. 267–270, Jul 1979. `10.1103/physrevlett.43.267`.

[22] P. Chen, J. M. Dawson, R. W. Huff, and T. Katsouleas, "Acceleration of electrons by the interaction of a bunched electron beam with a plasma," *Phys. Rev. Lett.*, vol. 54, pp. 693–696, Feb 1985. `https://link.aps.org/doi/10.1103/PhysRevLett.54.693`.

[23] R. Ischebeck, *Illustration: Plasma Wakefield Acceleration*. English Wikipedia, May 2011. `https://upload.wikimedia.org/wikipedia/commons/7/76/Illustration_Plasma_Wakefield_Acceleration.png`.

[24] A. Mukherjee, "Wave breaking field of relativistically intense electrostatic waves in electronegative plasma with super-thermal electrons," *Scientific Reports*, vol. 12, Jul 2022. `10.1038/s41598-022-16481-z`.

[25] J. M. Dawson, "Nonlinear electron oscillations in a cold plasma," *Physical Review*, vol. 113, p. 383–387, Jan 1959. `10.1103/physrev.113.383`.

[26] A. Caldwell, K. Lotov, A. Pukhov, and F. Simon, "Proton-driven plasma-wakefield acceleration," *Nature Physics*, vol. 5, p. 363–367, Apr 2009. `10.1038/nphys1248`.

[27] N. Kumar, A. Pukhov, and K. Lotov, "Self-modulation instability of a long proton bunch in plasmas," *Phys. Rev. Lett.*, vol. 104, p. 255003, Jun 2010. https://link.aps.org/doi/10.1103/PhysRevLett.104.255003.

[28] L. Verra *et al.*, "Development of the self-modulation instability of a relativistic proton bunch in plasma," *Phys. Plasmas*, vol. 30, no. 8, p. 083104, 2023. 10.1063/5.0157391.

[29] M. Wing, "Advanced wakefield experiment (awake)," *UCL Advanced Wakefield Experiment (AWAKE)*. `https://www.hep.ucl.ac.uk/awake/`.

[30] F. Batsch, "Transition between instability and seeded self-modulation of a relativistic particle bunch in plasma," *Phys. Rev. Lett.*, vol. 126, p. 164802, Apr 2021. https://link.aps.org/doi/10.1103/PhysRevLett.126.164802.

[31] L. Verra, G. Z. D. Porta, E. Gschwendtner, M. Bergamaschi, and P. Muggli, "Techniques to seed the self-modulation instability of a long proton bunch in plasma," 2023.

[32] P. San Miguel Claveria, E. Adli, L. D. Amorim, W. An, C. E. Clayton, S. Corde, S. Gessner, M. J. Hogan, C. Joshi, O. Kononenko, and et al., "Betatron radiation and emittance growth in plasma wakefield accelerators," *Philosophical Transactions of the Royal Society A: Mathematical, Physical and Engineering Sciences*, vol. 377, Jun 2019. `10.1098/rsta.2018.0173`.

[33] C. A. Lindstrøm, J. Beinortaitė, J. Björklund Svensson, L. Boulton, J. Chappell, S. Diederichs, B. Foster, J. M. Garland, P. González Caminal, G. Loisch, F. Peña, S. Schröder, M. Thévenet, S. Wesch, M. Wing, J. C. Wood, R. D'Arcy, and J. Osterhoff, "Emittance preservation in a plasma-wakefield accelerator," *Nature Communications*, vol. 15, p. 6097, Jul 2024. `https://doi.org/10.1038/s41467-024-50320-1`.

[34] E. Gschwendtner and P. Muggli, "Plasma wakefield accelerators: review," *Nature Reviews Physics*, vol. 1, p. 246–248, Mar 2019. `10.1038/s42254-019-0049-z`.

[35] E. Adli, A. Ahuja, O. Apsimon, R. Apsimon, A.-M. Bachmann, D. Barrientos, F. Batsch, J. Bauche, V. K. Berglyd Olsen, M. Bernardini, and et al., "Acceleration of electrons in the plasma wakefield of a proton bunch," *Nature*, vol. 561, p. 363–367, Aug 2018. `10.1038/s41586-018-0485-4`.

[36] R. Keinigs and M. E. Jones, "Two-dimensional dynamics of the plasma wakefield accelerator," *The Physics of Fluids*, vol. 30, p. 252–263, Jan 1987. `10.1063/1.866183`.

[37] C. L. O'Connell, *Plasma production via field ionization.* PhD thesis, SLAC, 2005.

[38] J. Kaiser and S. Chalk, "Oxidation state," *International Union of Pure and Applied Chemistry (IUPAC)*, 2019. `https://doi.org/10.1351/goldbook.004365`.

[39] S. Gessner and the AWAKE Collaboration, "Evolution of a plasma column measured through modulation of a high-energy proton beam," 2020. `https://arxiv.org/abs/2006.09991`.

Appendices

A Access to Data

The data included in this report was taken as a part of the AWAKE experiment at CERN. To respect CERN's open science policy, which includes *"open access to research publications, data, software and hardware [...]"* as stated on `https://openscience.cern/policies`, the data used in this thesis, as well as the code used to analyse the data is accessible upon request. The experimental logbook pdf can also be found there.
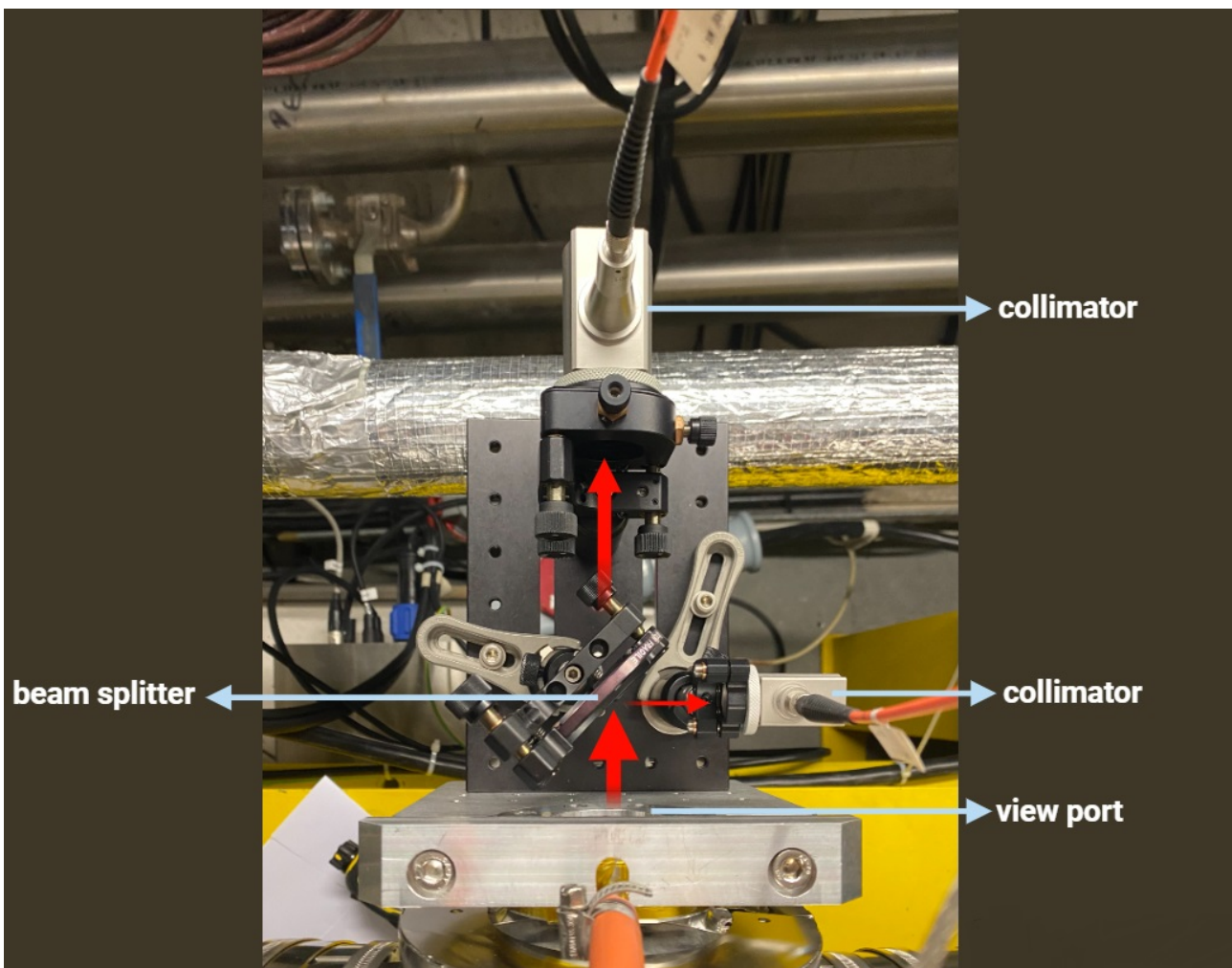
B Experimental Setup

Figure 18: A photo of the experimental setup for spectrometry of the plasma light. The relevant components are labelled. The light is shown in red, with the thicknes of the arrows representing the amount of light.
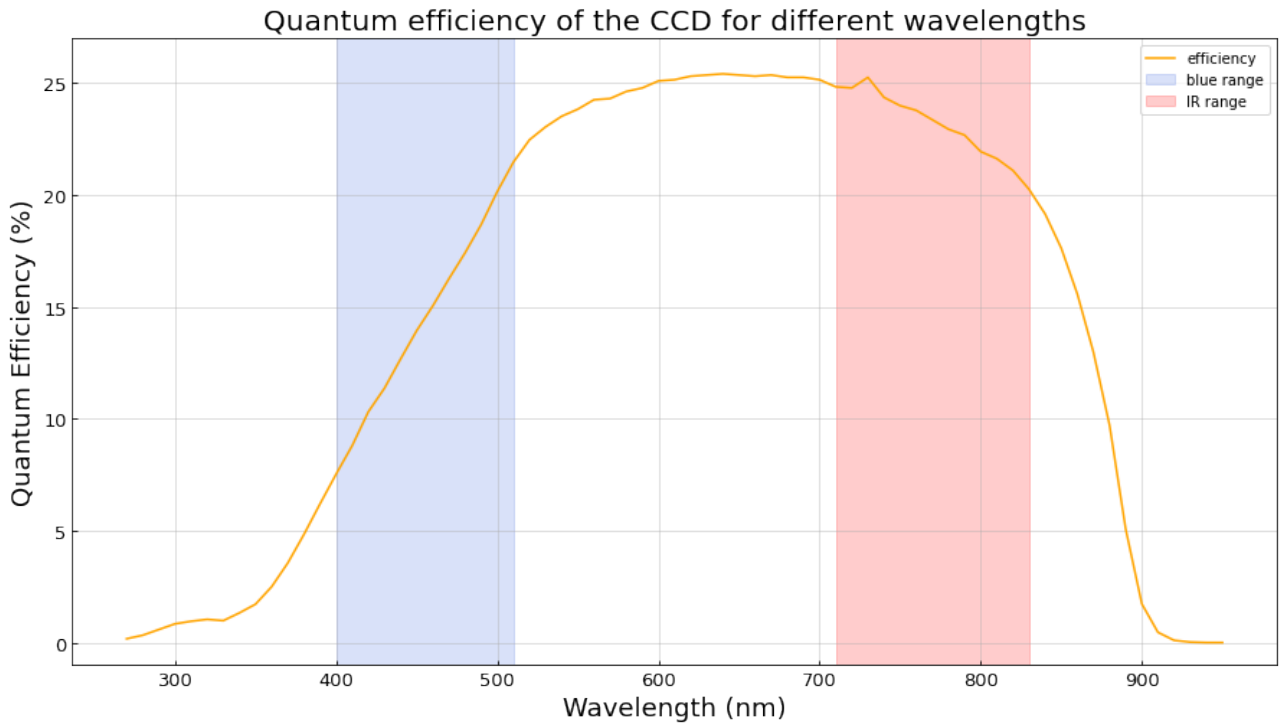
Figure 19: Efficiency of the camera for the range of wavelengths observed. The two ranges (blue and IR) are highlighted. The data was requested from the manufacturer.
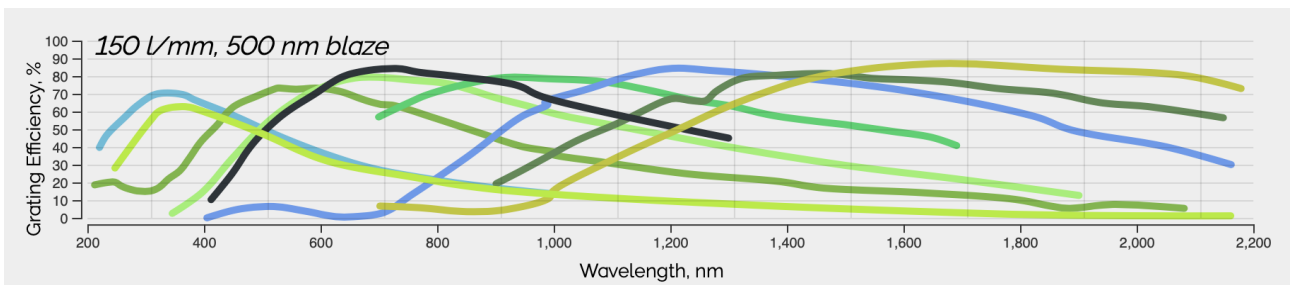

Figure 20: Efficiency curves for the spectrograph grating. The curve for the grating used is the third from the left.

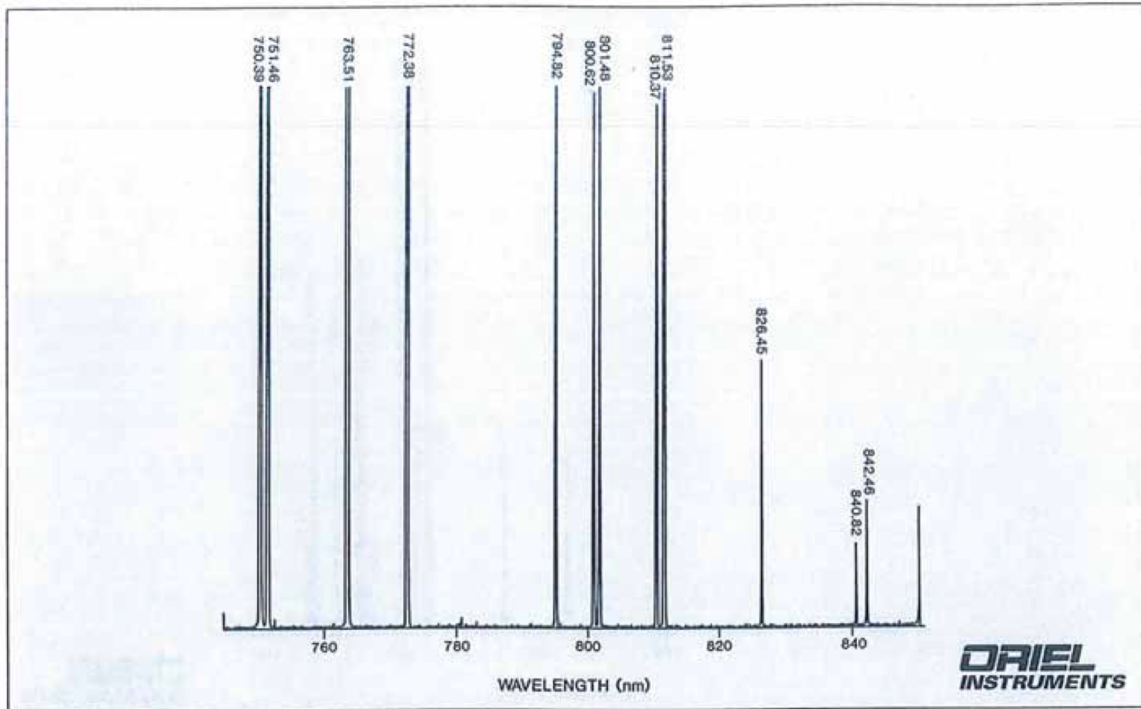# C Calibration of the Spectrograph

Fig. 3 Typical line output of 6030 Argon Lamp. Relative intensities vary with operating conditions.
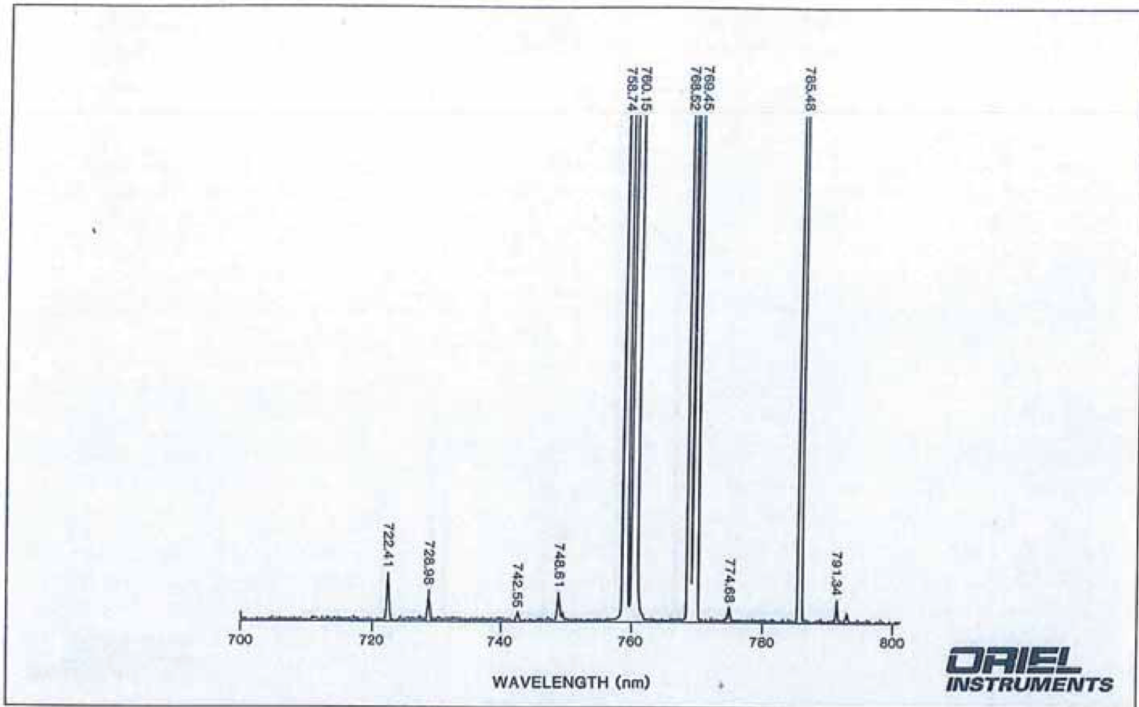
Figure 21: Typical spectrum of an Argon lamp.

Fig. 9 Typical line output of 6031 Krypton Lamp. Relative intensities vary with operating conditions.

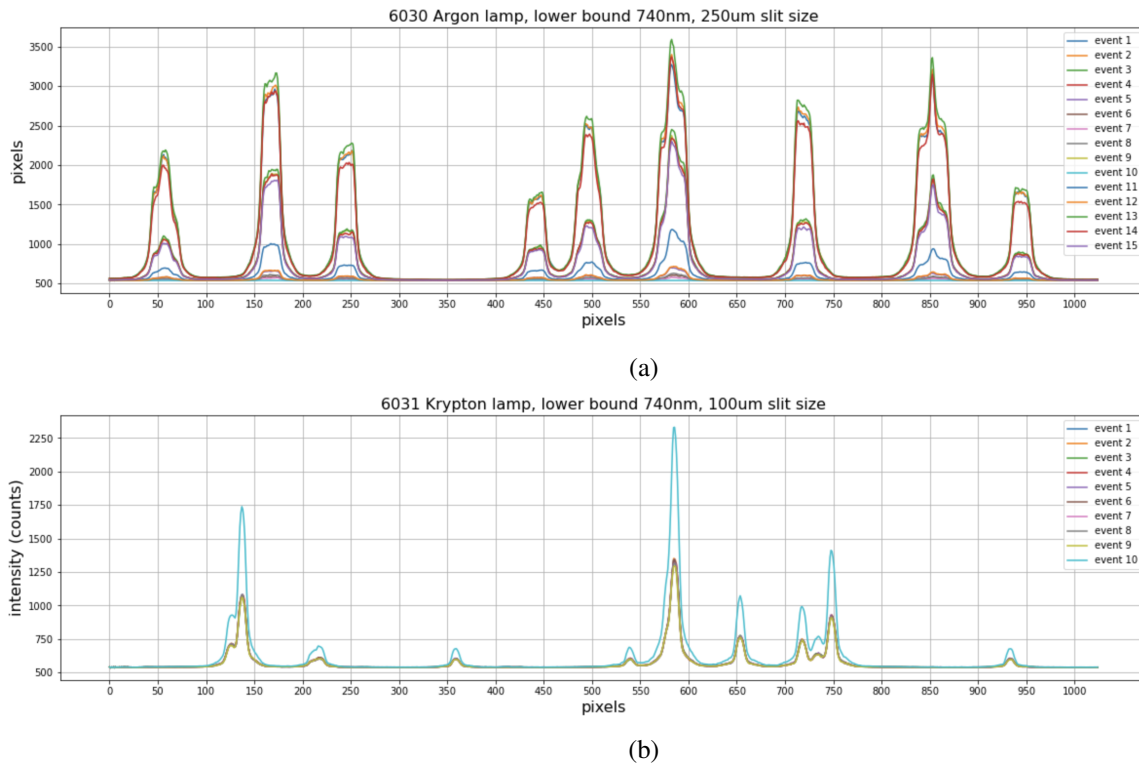Figure 22: Typical spectrum of a Krypton lamp.

(a)

(b)

Figure 23: (a) Observed spectrum of an Argon lamp in the range from 740 nm onwards. (b) Observed spectrum of a Krypton lamp in the range from 740 nm onwards.

D   Wakefield Amplitude Calculation Code

```python
import numpy as np
import matplotlib.pyplot as plt
import scipy.special as special
from scipy.integrate import quad
import scipy.constants

#constants
e = -scipy.constants.e #charge
e0 = scipy.constants.epsilon_0
sigma_r = 150e-6 #proton bunch radius
sigma_z = 0.007 #proton bunch length
n = 7e20
pInt = 3e10 #proton bunch charge
cpeed = scipy.constants.c #speed of light
#volume of a gaussian proton bunch
volGaus = (2*np.pi)**(3/2)*sigma_r**2*sigma_z
#wavevector of the plasma electron wave
kpe = np.sqrt((e**2 * n) / (e0 * scipy.constants.m_e))/cpeed
mean_z =0 #centre of the proton bunch, longitudinally

#functions

def radial_gaussian(x, sd, a=1, mean = 0):
    #returns a gaussian function, meant to be used as the radial bunch profile
    return (a)*np.exp( -(x - mean)**2 / (2*sd**2) )

```
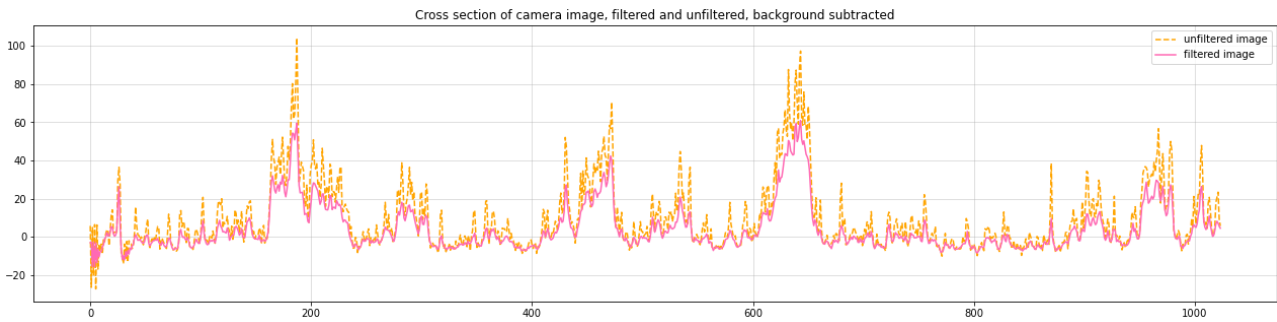
Figure 24: An example of a background-subtracted spectrum obtained from the camera.

```python
def long_gaussian(x, sd, mean=0):
    #returns a gaussian function, meant to be used as the longitudinal bunch
    profile
    return (pInt/volGaus)*np.exp( -(x - mean)**2 / (2*sd**2) )

def bessel_i(x):
    #returns the value of the modified Bessel function of the first kind, n=0
    return special.i0(x)

def bessel_i1(x):
    #returns the value of the modified Bessel function of the first kind, n=1
    return special.i1(x)

def bessel_k(x):
    #returns the value of the modified Bessel function of the second kind, n=0
    return special.k0(x)

def bessel_k1(x):
    #returns the value of the modified Bessel function of the second kind, n=1
    return special.k1(x)

def r_int1(r):
    #returns the value of the first integral in the R(r) formula, r is radial
    coordinate of the beam
    int_1 = r * radial_gaussian(r, sigma_r) * bessel_i(kpe * r)
    return int_1

def r_int2(r):
    #returns the value of the second integral in the R(r) formula, r is radial
    coordinate of the beam
    int_2 = r * radial_gaussian(r, sigma_r) * bessel_k(kpe * r)
    return int_2

def e_z(x):
    """
    returns the integral part of the formula for the longitudinal wakefield
    inputs:
    x : the position along the bunch
    xi: the position of the Relatiistic Ionisation Front (RIF)
    """
    e_cos = long_gaussian(x, sigma_z) * np.cos(kpe*(xi-x))
    return e_cos
```

```python
67  def e_rad(x):
68      """
69      returns the integral part of the formula for the transverse wakefield
70      inputs:
71      x : the position along the bunch
72      xi: the position of the Relatiistic Ionisation Front (RIF)
73      """
74      e_sin = long_gaussian(x, sigma_z) * np.sin(kpe*(xi-x))
75      return e_sin
76
77  def r_of_r(x):
78      """
79      Function returns the value of R(r) at certain x (r in the formula, denoted
        by x here)
80      The function integrates the first two lines from 0 to the chosen x and from
        the x to infinity
81      After that, it evaluates the rest of the function at x
82      """
83      int1 = lambda r: r * radial_gaussian(r, sigma_r) * bessel_i(kpe * r)
84      int2 = lambda r: r * radial_gaussian(r, sigma_r) * bessel_k(kpe * r)
85      #integral = kpe**2 * quad(r_int1, 0, x)[0] * bessel_k(x * kpe) + kpe**2 *
        quad(r_int2, x, sigma_r*100)[0] * bessel_i(x * kpe)
86      integral = kpe**2 * quad(int1, 0, x)[0] * bessel_k(x * kpe) + kpe**2 * quad(
        int2, x, np.inf)[0] * bessel_i(x * kpe)
87      return integral
88
89  def dRdr(x):
90      """
91      Function returns the value of dR(r)/dr at a certain 'x' value of radius
92      Function integrates the first two lines using x in the limit, then evaluates
         the function at the given x
93      """
94      int1 = lambda r: r * radial_gaussian(r, sigma_r) * bessel_i(kpe * r)
95      int2 = lambda r: r * radial_gaussian(r, sigma_r) * bessel_k(kpe * r)
96
97      dRdr = -kpe**3 * bessel_k1(kpe * x) * quad(int1, 0, x)[0] +\
98          + kpe**2 * bessel_k(kpe * x) * x * radial_gaussian(x, sigma_r) *
        bessel_i(kpe * x) +\
99          + kpe**2 * bessel_i(kpe * x) * x * radial_gaussian(x, sigma_r) *
        bessel_k(kpe * x) +\
100         + (-1) * kpe**3 * bessel_i1(kpe * x) * quad(int2, x, x*100)[0]
101     return dRdr
102
103 def wak_z(xi, r, rif):
104     """
105     Function finds the amplitude of longitudinal wakefields at some point in the
         bunch
106     inputs:
107     xi: longitudinal distance in the bunch
108     r: radial distance from the z axis
109     rif: position of the relativistic ionisation front
110     """
111     e_cos = lambda x: long_gaussian(x, sigma_z, rif) * np.cos(kpe*(xi-x))
112     #e_cos = lambda x: (long_gaussian(x, sigma_z, rif)* (1 + random.randint
        (-10,10)/1000)) * np.cos(kpe*(xi-x))
113
114     return (e/e0) * quad(e_cos, 0, xi)[0] * r_of_r(r)
```

```python
115
116  def wak_r(xi, r, rif):
117      """
118      Function finds the amplitude of transverse wakefields at some point in the
     bunch
119      inputs:
120      xi: longitudinal distance in the bunch
121      r: radial distance from the z axis
122      rif: position of the relativistic ionisation front
123      """
124      #e_sin = lambda x: (long_gaussian(x, sigma_z, rif)* (1 + random.randint
     (-10,10)/1000)) * np.sin(kpe*(xi-x))
125      e_sin = lambda x: long_gaussian(x, sigma_z, rif) * np.sin(kpe*(xi-x))
126
127      return (e / (e0 * kpe)) * quad(e_sin, 0, xi)[0] * dRdr(r)
```

E   All Observed Rubidium Lines

Table 4: Rubidium lines that were used in the data analysis as the "blue range". The table shows the observed wavelength, the line wavelength from NIST and the energy levels for the transition.

λ[nm]	NIST λ	lower level	upper level
424	424.44	$4p^5(^2P^\circ_{3/2})5s$, J= 2	$4p^5(^2P^\circ_{3/2})5p$, J= 3
427	427.31	$4p^5(^2P^\circ_{3/2})5s$, J= 2	$4p^5(^2P^\circ_{3/2})5p$, J= 2
437	437.71	$4p^5(^2P^\circ_{3/2})5p$, J= 3	$4p^5(^2P^\circ_{3/2})6s$, J= 2
456	457.18	$4p^5(^2P^\circ_{3/2})5s$, J= 1	$4p^5(^2P^\circ_{3/2})5p$, J= 2
464	464.86	$4p^54d$	$4p^5(^2P^\circ_{3/2})5p$, J= 2
477	477.59	$4p^5(^2P^\circ_{3/2})5s$, J= 2	$4p^5(^2P^\circ_{3/2})5p$, J= 1
514	515.21	$4p^5(^2P^\circ_{3/2})5s$, J= 1	$4p^5(^2P^\circ_{3/2})5p$, J= 1

Table 5: Rubidium lines that were used in the data analysis as the "IR range". The table shows the observed wavelength, the line wavelength from NIST and the energy levels for the transition.

λ[nm]	NIST λ	lower level	upper level
727	727.99	$4p^65p$, J=1/2	$4p^67s$, J= 1/2
740	740.82	$4p^65p$, J=3/2	$4p^67s$, J=1/2
760	761.89	$4p^65p$, J=1/2	$4p^65d$, J=3/2
775	775.77	$4p^65p$, J=3/2	$4p^65d$, J=5/2
780	780.03	$4p^65s$, J=1/2	$4p^65p$, J=3/2
794	794.76	$4p^65s$, J=1/2	$4p^65p$, J=1/2